Thesis for the Degree of Licentiate of Engineering

Integrated Nonlinear Optics in Silicon Nitride Waveguides

Clemens Krückel

Photonics Laboratory
Department of Microtechnology and Nanoscience (MC2)
Chalmers University of Technology
Göteborg, Sweden, 2015

Integrated Nonlinear Optics in Silicon Nitride Waveguides

Clemens Krückel

Göteborg, December 2015

Technical Report MC2-324
ISSN 1652-0769

Chalmers University of Technology
Microtechnology and Nanoscience (MC2)
Photonics Laboratory
SE-412 96 Göteborg, Sweden
Phone: +46 (0) 31 772 1000

Printed by Chalmers reproservice, Chalmers University of Technology
Göteborg, Sweden, December, 2015

Integrated Nonlinear Optics in Silicon Nitride Waveguides

Clemens Krückel

Chalmers University of Technology
Department of Microtechnology and Nanoscience (MC2)
Photonics Laboratory, SE-412 96 Göteborg, Sweden

Abstract

Integrated optics platforms offer the possibility to implement compact photonic devices for nonlinear optics applications. Modern nanofabrication facilities allow the fabrication of sub-micron-sized waveguide geometries that confine light to reach very high optical intensities. These intensities enable efficient nonlinear processes that are further enhanced by using materials with high nonlinear Kerr coefficients. Additionally, dispersion engineering by changing the waveguide dimensions allows for broadband operation.

In this thesis, we explored silicon nitride as the core material of silica embedded waveguides. Silicon nitride does not show nonlinear loss constraints, which makes this material very suitable for high optical intensities. The material has a large transparency window, from the ultraviolet to the short-wave infrared, and it is completely compatible with CMOS fabrication standards. The potential of this platform for diverse linear and nonlinear optics applications has been demonstrated before.

We studied two slightly distinct material platforms: stoichiometric silicon nitride, Si_3N_4, and non-stoichiometric silicon nitride, Si_xN_y. The accessible Si_3N_4 material platform consisted of thin low-confinement waveguides with low propagation loss of 0.06 dB/cm and a moderate nonlinear coefficient of 285 $(W{\cdot}km)^{-1}$. In a 1 m long waveguide the nonlinear performance was studied experimentally. The realized four-wave mixing (FWM) experiment showed a conversion efficiency of -26.1 dB and ultrafast all optical signal processing was demonstrated by wavelength conversion of high-speed data. The Si_xN_y material was processed to realize thick high-confinement waveguides that show propagation loss of around 1 dB/cm and a nonlinear coefficient of 6100 $(W{\cdot}km)^{-1}$. The material specific nonlinear Kerr coefficient was $1.4{\cdot}10^{-18}$ m^2/W, which is five times higher than Si_3N_4. With this material platform the fabrication of thick layers up to 700 nm in a single deposition step was demonstrated, a procedure not possible in Si_3N_4. The thick layers enable broadband dispersion engineering.

Keywords: four-wave mixing, integrated optics devices, nanostructure fabrication, nonlinear optical signal processing, nonlinear optics, semiconductor materials, wavelength conversion devices

List of papers

This thesis is based on the following appended papers:

[A] **C. J. Krückel**, V. Torres-Company, P. A. Andrekson, D. T. Spencer, J. F. Bauters, M. J. R. Heck, and J. E. Bowers, “Continuous wave-pumped wavelength conversion in low-loss silicon nitride waveguides,” *Optics Letters*, vol. 40, no. 6, pp. 875-878, 2015.

[B] **C. J. Krückel**, A. Fülöp, T. Klintberg, J. Bengtsson, P. A. Andrekson and V. Torres-Company, “Linear and nonlinear characterization of low-stress high-confinement silicon-rich nitride waveguides,” *Optics Express*, vol. 23, no. 20, pp. 25828-25837, 2015.

Related publications and conference contributions by the author not included in the thesis:

Journal papers

[C] A. Fülöp, **C. Krückel**, D. Castelló Lurbe, E. Silvestre and V. Torres-Company, "Triply resonant coherent four-wave mixing in silicon nitride microresonators," *Optics Letters*, vol. 40, no. 17, pp. 4006-4009, 2015.

Conference presentations and papers

[D] **C. Krückel**, V. Torres-Company, P. Andrekson, J. Bovington, J. Bauters, M. Heck and J. Bowers, "Continuous-wave nonlinear optics in low-stress silicon-rich nitride waveguides," *Proceedings of the Conference on Lasers and Electro-Optics*, 2014.

[E] **C. Krückel**, A. Fülöp, P. Andrekson and V. Torres-Company, "Continuous-wave nonlinear optics in low-stress silicon-rich nitride waveguides," *Optical Fiber Communication Conference W1K.4*, 2015.

Acknowledgement

I would like to thank Prof. Peter Andrekson for giving me the opportunity to gain experience and improve my professional skills in the research environment in the photonics laboratory. I acknowledge Prof. Magnus Karlsson for sharing his expertise and answering questions about nonlinear optics.
I want to thank my supervisor Dr. Víctor Torres-Company for being a thorough and talented leader.
I would like to acknowledge Prof. John Bowers, Dr. Jared Bauters, Dr. Martijn Heck and Daryl Spencer from the University of California Santa Barbara for providing waveguide samples. In order to establish our own processing line, I was highly supported with expertise from the MC2 cleanroom staff. I would like to thank in particular Johan Andersson, Mats Hagberg, Karin Hedsten, Göran Alestig and Ulf Södervall for their valuable support.
I thank my colleague Dr. Erik Haglund for sharing his snus with me but more importantly his profound knowledge about nanofabrication. Attila Fülöp deserves acknowledgment for fruitful discussions about integrated optics and letting me utilize his mature computer skills now and then.
I have to thank my three office mates gratefully. Dr. Josué Parra Cetina for being a great fellow, Dr. Samuel Olsson for his organized manner of answering any question and Dr. Vicente Durán Bosch for his Spanish education and positive approach towards Mondays. Special thanks are also directed to Dr. Aleš Kumpera, Tobias Eriksson and Tamás Lengyel for being around and making work more harmonic and joyful.
Furthermore, I extend thanks to Jeanette Träff for being supportive and I acknowledge of course all the rest of the photonics laboratory members for being great colleagues.
Finally, I want to express gratitude to all my family and friends.

Clemens Krückel

Göteborg
December 2015

This work was financially supported by the European Research Council Advanced Grant PSOPA (291618) and the Swedish Research Council (VR).

Abbreviations

ChGs chalcogenide glasses

CMOS complementary metal-oxide-semiconductor

CVD chemical vapor deposition

CW continuous wave

DUV deep ultraviolet

ebeam electron-beam

EUV extreme ultraviolet

FCA free carrier absorption

FWM four-wave mixing

GVD group-velocity dispersion

HNLF highly nonlinear fiber

IC integrated circuit

IR infrared

LPCVD low-pressure chemical vapor deposition

MBE molecular beam epitaxy

MEMS micro-electro-mechanical systems

MOCVD metalorganic chemical vapor deposition

MOSFET metal-oxide-semiconductor field-effect transistor

NA numerical aperture

PECVD plasma-enhanced chemical vapor deposition

RF radio frequency

RIE reactive-ion etching

SBS stimulated Brillouin scattering

SHG second-harmonic generation

SOA semiconductor optical amplifier

SOI silicon-on-insulator

SPM self-phase modulation

SSMF standard single-mode fiber

THG third-harmonic generation

TPA two-photon absorption

UV ultraviolet

VCSEL vertical-cavity surface-emitting laser

XPM cross-phase modulation

Contents

Chapter 1

Introduction

Our society displays a huge demand for high-speed internet. This demand is satisfied by the technological achievements made in the field of optical communication. This field involves the transmission of digital information via light over fibers of glass. Thereby, light is routed through a global network of optical fibers in order to connect computers and data centers all over the world. With the advent of fiber technology in 1966 [1], modern communication became revolutionized leading to fiber links with outstanding data rates beyond 1 Tb/s.

The optical fiber is the general data transmission medium used in long distance connections of metro and long-haul links between cities and continents, but also in connections of shorter range, like in data centers or supercomputers. Indeed, the fiber has progressively replaced most metal-based transmission lines (e.g. copper) for distances down to 1 m [2]. Interestingly, it was already predicted in 1984 [3] that the optical connection is the best solution to connect silicon electronic components. The reason for this is that an optical connection has about six orders of magnitude lower loss at high data speeds compared to an electrical connection.

Data centers are huge facilities for data storage and data processing driven by social media platforms or search engines. The large number of servers in a data center are commonly linked by fiber-based optical interconnects [2]. There are two current methods to realize an optical interconnect, utilizing vertical-cavity surface-emitting lasers (VCSELs) or silicon photonics. Before introducing these two technologies, the invention of the laser in 1960 [4] should be acknowledged which is the fundamental key component that enables optical communication. The VCSEL, based on III-V materials, is a laser source that offers high-speed direct on-off switching to modulate binary optical data [5, 6].

Companies like TE connectivity utilize the VCSEL technology in their optical interconnects to reach data rates of 25.75 Gb/s [7]. The silicon photonics approach on the other hand utilizes an external laser in combination with a silicon based modulator integrated on a microchip. Recently Luxtera has presented their 4·10 Gb/s transceiver based on silicon photonics technology [8]. The major requirements for the platforms used in data centers are low-cost fabrication, low-power consumption, high reliability and simple scalability to higher data rates. In [9] both platforms, VCSEL and silicon photonics, are compared regarding the technological and economic performance. The prediction foresees that silicon photonics is favored for longer connections with single-mode fibers and VCSELs continue its domination for data centers due to economical benefits.

In the context of this thesis, it is meaningful to present the field of silicon photonics in more detail. Silicon photonics is the integration of optical devices on a silicon microchip. For the integration of optical devices the same nanofabrication facilities are utilized as for the high volume integration of silicon microelectronics. Silicon microelectronics, more precisely the complementary metal-oxide-semiconductor (CMOS) transistor logic, is the central key figure leading to the information revolution in the last 50 years. Especially noticeable is massive size reduction and performance increase of electronic devices. With the integration of the first optical waveguide in silicon in 1986 [10], it was proven that the fabrication environment for silicon electronics can also be utilized to manufacture optical devices. In 1996 a rib waveguide was presented using the silicon-on-insulator (SOI) platform with low losses of 0.1 dB/cm showing the potential of light guiding on chip [11]. This shows that within silicon photonics even optical interconnects between processor cores at the microchip level is possible [2]. Unfortunately, silicon has no efficient light emission so by now only hybrid solutions are available where III-V lasers are bonded on the silicon photonics chip [12].

Nevertheless, thanks to the compatibility with CMOS fabrication facilities, tailored for high-volume low-cost processing, the fabrication of silicon photonic circuits in the same process line offers many advantages. Additionally it offers the opportunity to bring together optics and electronics on the same microchip. One interesting change in recent years is the offered access to silicon photonic systems for researchers without fabrication facilities in the context of a multi-project wafer runs [13]. Here production costs are shared by combining designs on the same wafer that is manufactured in large quantities for all users. With multi-project wafer runs the fabless access to silicon photonics components becomes affordable [13].

By utilizing external fabless fabrication or in-house fabrication, crystalline silicon has become a common material of choice for integrated optics. Over the past years the research output in the field of silicon photonics for linear optical

applications has increased. Howerver, it turns out that silicon is also a very promising material for nonlinear optics applications [14]. A high refractive index and huge nonlinearities are the major advantages of this material for nonlinear integrated optics. The small core dimensions achievable with modern fabrication in combination with high index contrast to silica as a cladding material lead to remarkably high optical confinement, with huge intensities that enable efficient nonlinear processes. The nonlinear optical effects can be utilized for applications like signal regeneration [15], broadband wavelength conversion [16] or supercontinuum generation [17]. However, nonlinear loss contributions that occur for wavelengths in telecommunication bands limit the performance of this material platform [18, 19].
A material platform that overcomes these challenges and does not show nonlinear losses at telecommunication wavelengths because of its large optical bandgap is silicon nitride [20]. Silicon nitride is also a CMOS-compatible material [21] and offers the same potential for mass production. Similar to silicon, silicon nitride is accessible for the broader research community through multi-project wafer runs. In its stoichiometric composition, Si_3N_4, waveguides with extraordinary low-loss performance down to 0.001 dB/cm have been demonstrated [22]. It has a fairly high nonlinear Kerr coefficient [23]. Impressive demonstrations in nonlinear optics include octave spanning comb generation [24] and ultra-broad supercontinuum generation [25]. However, fabrication challenges to achieve thick waveguides constrains the important capabilities for dispersion engineering as thick films show cracks due to high tensile stress [26].
With the increase of the silicon content in the silicon nitride film, the material becomes non-stoichiometric silicon nitride Si_xN_y and the tensile stress can be relaxed, offering the opportunity to achieve thick layers [27]. In this thesis the focus is directed on the investigation of thin stoichiometric silicon nitride waveguides and crack-free thick non-stoichiometric silicon nitride waveguides for the field of nonlinear integrated optics.

1.1 This thesis

In this thesis we present two silicon nitride based waveguide platforms. In Paper A we present low-loss low-confinement waveguides fabricated from stoichiometric silicon nitride. Here we show that the nonlinear performance in Si_3N_4 waveguides is similar compared to silicon waveguides without free-carrier removal. As the dispersion engineering capabilities are limited in the thin low-confinement waveguides cores, thick films are favorable. The limitations to deposit thick stoichiometric silicon nitride is the motivation of this thesis to explore low-stress non-stoichiometric silicon nitride. In Paper B we demonstrate that silicon-rich nitride can be used to fabricate thick crack-free films up to 700 nm but with the downside of increased waveguide losses.

Thesis outline
In chapter 2 the effects of nonlinear optics are explained with a focus on χ^3-based Kerr nonlinearities like four-wave mixing (FWM). Chapter 3 covers the basics about waveguide theory including information about mode properties, loss and coupling mechanisms of waveguides. In chapter 4 common material platforms for integrated nonlinear optics are introduced. The platforms are compared in terms of linear and nonlinear performance and benchmarked with the highly-nonlinear fiber (HNLF) technology. Chapter 5 includes the presentation of CMOS-compatible fabrication techniques that are used to manufacture optical waveguides. In Chapter 6 possible future projects are discussed.

Chapter 2

Nonlinear Kerr optics

For high optical intensities the interaction of light and matter becomes nonlinear, meaning that the optical radiation after propagation through a medium is not a linear superposition of the radiation before the medium. Especially when working with integrated optics, a very high confinement of light can be achieved leading to very high intensities. The resulting nonlinear effects can be utilized for useful applications. In this chapter the fundamental physical principles for nonlinear interaction of light and matter are explained with a focus on nonlinear Kerr optics, the dominant nonlinear effect in materials used for integrated optics.

2.1 Nonlinear polarization and refraction

The propagation of electromagnetic radiation is described by Maxwell's equations. In a transparent medium with no free charges Maxwell's equations become

$$\nabla \times \mathbf{E} = -\frac{\partial \mathbf{B}}{\partial t} \tag{2.1}$$

$$\nabla \times \mathbf{H} = \frac{\partial \mathbf{D}}{\partial t} \tag{2.2}$$

$$\nabla \cdot \mathbf{D} = 0 \tag{2.3}$$

$$\nabla \cdot \mathbf{B} = 0, \tag{2.4}$$

where $\mathbf{E}$ and $\mathbf{H}$ are the electric and magnetic field vectors, and $\mathbf{D}$ and $\mathbf{B}$ are the electric and magnetic flux densities [28]. The interaction of light with the medium is described by the electric displacement of charges $\mathbf{D}$ given by

$$\mathbf{D} = \epsilon_0 \mathbf{E} + \mathbf{P}, \tag{2.5}$$

where ϵ_0 is the vacuum permittivity and $\mathbf{P}$ is the induced polarization of the medium. The polarization of the material describes the reorientation and relocation of charges and dipoles in response to a present electric field. As the light has vector nature, the susceptibility terms are tensors and the material response depends on its orientation and isotropy. To provide a simple physical insight, a scalar mathematical description is chosen from here on.
For a low electric-field strength in an isotropic medium, the polarization follows a linear dependence

$$P_{\mathrm{lin}} = \epsilon_0 \chi E, \tag{2.6}$$

where ϵ_0 is the vacuum permittivity and the susceptibility χ is the proportionality factor. The susceptibility χ is related to the relative electrical permittivity of the medium ϵ by $\chi = \epsilon - 1$. The refractive index n_0 of the material is connected to the electrical permeability by $\mathrm{n}_0 = \sqrt{\frac{\epsilon}{\epsilon_0 \mu_0}}$, with μ_0 as the vacuum permeability.
For intense electrical fields a saturation of the polarization takes place and the polarization response of the material becomes nonlinear. The nonlinear polarization behavior at high intensities has its origin in the nonlinearity of the motion of molecular bound electrons in the material. The description of the polarization including nonlinear behavior is described by a pertubative approach [28]

$$P = P_{\mathrm{lin}} + P_{\mathrm{nl}} = \epsilon_0 \chi E + \epsilon_0 \chi^{(2)} E^2 + \epsilon_0 \chi^{(3)} E^3 + \dots \quad . \tag{2.7}$$

Here $\chi^{(2)}$ and $\chi^{(3)}$ are the second and third-order susceptibility leading to the second and third-order nonlinear polarization terms. As the higher-order susceptibility terms are in general several orders of magnitude smaller than the linear susceptibility, they only become effective at high intensities. Different susceptibility terms contribute to particular optical effects and have influence on the interaction of radiation with matter. For example, the linear susceptibility χ is included in the refractive index n_0 of the material and accounts for the change of optical phase. In the case of a complex electrical permittivity ϵ of the medium, optical attenuation is accounted for by its imaginary part. The second-order susceptibility $\chi^{(2)}$ leads to effects like second-harmonic generation, sum-frequency generation or the linear electro-optic effect (Pockels' effect). The third-order susceptibility $\chi^{(3)}$ results in third-harmonic generation or the quadratic electro-optic effect (Kerr effect) [29].

The Kerr effect is of large interest in this thesis. It is common to describe the strength of this effect with the nonlinear Kerr coefficient n_2 that is related to the third-order susceptibility by $n_2 = \frac{3}{4}\frac{\chi^{(3)}}{c\epsilon_0^2}$ [30]. The effect leads to nonlinear refraction, where the refractive index of a material changes in the presence of light with high intensities. This intensity dependence of the refractive index is accounted for in [28]

$$n(\omega, |E|^2) = n_0(\omega) + n_2 |E|^2 , \tag{2.8}$$

where E is the electric field amplitude of a single frequency component. The frequency dependence of the linear refractive index expresses the dispersion of the material. As the phase shift of a wave is dependent on the refractive index, both the linear and the nonlinear part contribute to the total phase shift of a wave in a medium[1].

The nonlinear polarization of a material can give rise to generation of light at frequencies different from the one of the excitation field. Nonlinear polarization takes place in various materials of liquid, gaseous or solid state where solids may have amorphous or crystalline composition. It is important to mention that materials with molecular inversion symmetry do not posses even order susceptibility terms. This means that in materials like silicon or silicon dioxide the lowest nonlinear susceptibility term is $\chi^{(3)}$. The polarization response of the medium excited with a monochromatic electrical field is illustrated in Fig. 2.1. Here an excitation field of $E(t) = E_0 \cos(\omega_1 t)$ was used for convenience. For low intensity fields the polarization P follows the present field linearly without showing nonlinear behavior as shown in Fig. 2.1.a. The frequency of the output field only contains the component at ω_1 in relation to the excitation field. Increased intensities trigger the nonlinear response of the material polarization accounting for higher-order polarization terms. For a $\chi^{(2)}$-material the second-order polarization produces nonlinear distortion of the polarization. As shown in Fig. 2.1.b, the induced polarization does not follow the excitation field. This results in a new frequency component at $2\omega_1$ resulting from the squared field component in Eq. 2.7. Similar is the process in $\chi^{(3)}$-materials where a third-harmonic is produced at $3\omega_1$ driven by the third-order susceptibility illustrated in Fig. 2.1.c [31].

[1] In terms of nonlinear phase shift one distinguishes between self-phase modulation (SPM) and cross-phase modulation (XPM). SPM is when the nonlinear phase shift of a wave is self-induced by its intensity. XPM is the nonlinear phase shift induced by the intensity of light at other frequencies or polarization.

2.2 Four-wave mixing

In $\chi^{(3)}$-materials the polarization is given by

$$P = \epsilon_0 \chi E + \epsilon_0 \chi^{(3)} E^3, \tag{2.9}$$

where the third-order polarization term is included. This term involves the nonlinear interaction of four waves and leads to the phenomenon of FWM. This Kerr effect based phenomenon results from the radiation induced modulation of the refractive index as shown in Eq. 2.8 and causes the generation of light at new frequencies. In this context the medium is mediating the nonlin-

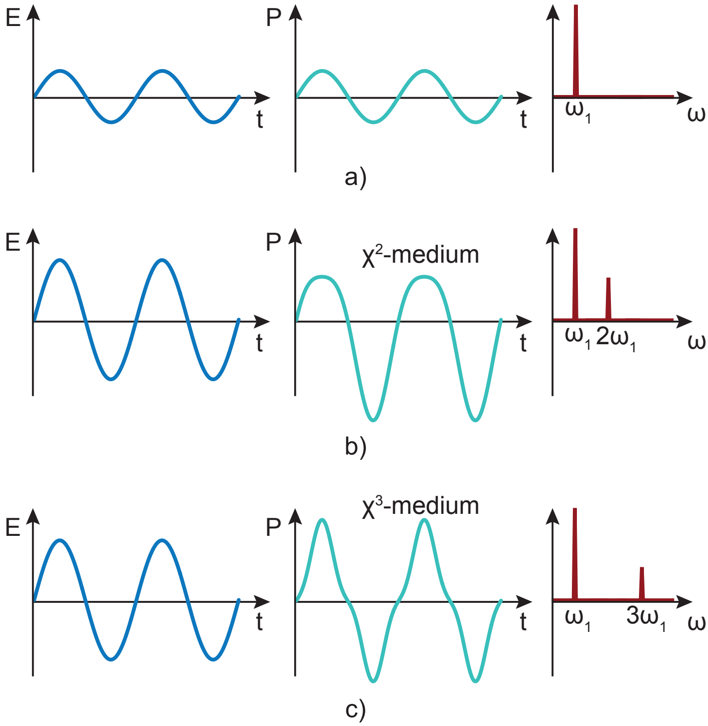

Figure 2.1: Illustration of material polarization P and frequency generation in dependence of the input field amplitude E and material susceptibility χ. a) Linear polarization of material. b) Nonlinear material polarization based on $\chi^{(2)}$ susceptibility. Second-harmonic frequency generation at $2\omega_1$. c) Nonlinear material polarization based on $\chi^{(3)}$ susceptibility. Third-harmonic frequency generation at $3\omega_1$.

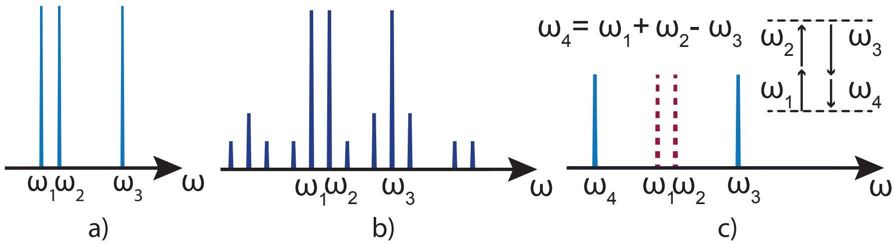

Figure 2.2: a) Illustration of spectrum with three waves at frequencies ω_1, ω_2 and ω_3. b) Illustration of frequency generation in the four-wave mixing process. c) Illustration of energy-conservation in the four-wave mixing process.

ear interaction among optical waves through elastic scattering of the material bound electrons where in principle no energy is absorbed by the medium. This means that the photon energy is conserved in this parametric process.

In order to exemplify the four-wave mixing process and the resulting generation of new frequency components, we consider the input to a $\chi^{(3)}$-material as a superposition of three monochromatic waves at different frequencies as shown in Fig. 2.2.a. The mixing term of the input waves is given by $E(t) = E_1\cos(\omega_1 t) + E_2\cos(\omega_2 t) + E_3\cos(\omega_3 t)$ that is inserted into Eq. 2.9. The triple product of E results in multiple new frequency components at the output. All possible new frequencies at the output of the medium are combinations of the input frequencies given by

$$
\begin{gathered}
(\omega_1 + \omega_2 - \omega_3), (\omega_1 + \omega_3 - \omega_2), (\omega_2 + \omega_3 - \omega_1), \\
(2\omega_1 \pm \omega_2), (2\omega_1 \pm \omega_3), \\
(2\omega_2 \pm \omega_1), (2\omega_2 \pm \omega_3), \\
(2\omega_3 \pm \omega_1), (2\omega_3 \pm \omega_1), \\
3\omega_1, 3\omega_2, 3\omega_3, (\omega_1 + \omega_2 + \omega_3).
\end{gathered}
$$

The frequency components that are generated in the FWM process are illustrated in Fig. 2.2.b (components around the third-order harmonics are not included in the figure). The efficiency of each of the above wave interactions depends on the phase-matching condition which will be explained in section 2.4. During the FWM process the photon energy of the four-waves interacting is conserved. To illustrate this, we focus on the generated frequency component at $\omega_4 = \omega_1 + \omega_2 - \omega_3$ as shown Fig. 2.2.c. Given the photon energy of $E_{photon} = \hbar\omega$, with $\hbar$ as the reduced Planck constant, the energy is conserved if energy is transferred from two photons at frequencies ω_1 and ω_2 to photons at the frequencies ω_3 and ω_4 satisfying $\omega_1 + \omega_2 = \omega_3 + \omega_4$.

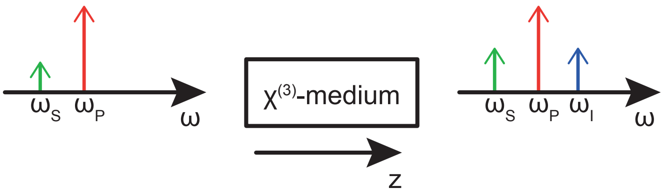

Figure 2.3: Illustration of the pump-degenerate FWM process. The propagation direction of the waves is indicated by z.

2.3 Wavelength conversion

Let us consider a common case in nonlinear optics in which the input to a $\chi^{(3)}$-material consists of a strong wave at ω_P, called the pump, and a weak one at ω_S called the signal. As the waves propagate through the medium the signal wave may be amplified and a wave at ω_I, called the idler, is generated, as illustrated in Fig. 2.3. This scenario is referred to as pump-degenerate FWM. The FWM process here is similar to the example given before where the generated new frequency at ω_4 satisfies the relation $\omega_4 = \omega_1 + \omega_2 - \omega_3$. In the pump-degenerate process both donated photons (ω_1 and ω_2) are at the same wavelength, in particular $\omega_1 = \omega_2 = \omega_P$, and the signal wave is at $\omega_3 = \omega_S$. This means that the energy conservation in the pump-degenerate FWM process is given by [28]

$$\omega_I = 2\omega_P - \omega_S \tag{2.10}$$

considering $\omega_4 = \omega_I$. The interaction between the pump, signal and idler waves as propagating along the z-direction is described via three coupled differential equations given by [28]

$$\frac{dE_p}{dz} = i\gamma\left\{\left[|E_p|^2 + 2\left(|E_s|^2 + |E_i|^2\right)\right]E_p + 2E_sE_iE_p^* \exp\left(i\Delta\beta z\right)\right\}, \tag{2.11}$$

$$\frac{dE_s}{dz} = i\gamma\left\{\left[|E_s|^2 + 2\left(|E_p|^2 + |E_i|^2\right)\right]E_s + E_i^*E_p^2 \exp\left(-i\Delta\beta z\right)\right\}, \tag{2.12}$$

$$\frac{dE_i}{dz} = i\gamma\left\{\left[|E_i|^2 + 2\left(|E_p|^2 + |E_s|^2\right)\right]E_i + E_s^*E_p^2 \exp\left(-i\Delta\beta z\right)\right\}. \tag{2.13}$$

The coupling between the waves is linked by the nonlinear parameter γ and the mismatch of the propagation constant between the waves $\Delta\beta$. It is assumed that the waves have the same optical polarization and optical field overlap. The nonlinear parameter γ includes the nonlinear effects in $\chi^{(3)}$-materials and the field confinement, which is explained in more detail in section 3.5. The mismatch of the propagation constant for pump, signal and idler wave is given by $\Delta\beta = 2\beta_P - \beta_S - \beta_I$ where the propagation constants of pump, signal and idler are given by β_P, β_S and β_I. The propagation constant β gives information about the velocity of a wave (more detail in section 3.3).

2.4 Phase-matching condition

For efficient energy transfer between the waves in the FWM process, the conservation of momentum is required. This means that the efficiency with which power is transferred depends on the relative phase among the interacting waves. This is described within the nonlinear phase-matching condition

$$\kappa \equiv \Delta\beta + 2\gamma P_p = 0, \tag{2.14}$$

where the linear part $\Delta\beta$ comes from the mismatch of the propagation constant between the waves and the nonlinear part $2\gamma P_p$ accounts for the nonlinear phase shift. This equation is valid under the assumption that no pump depletion takes place and the pump power is much larger than the signal and idler power so that the main contribution to the nonlinear phase shift comes from the pump. The factor of two accounts for the pump-degenerate FWM as both annihilated pump photons are located at the same frequency. In the coupled differential equations 2.11-2.13 the nonlinear and linear phase shifts are included in the first and second terms in the parenthesis [28]. In order to compensate for the positive nonlinear phase shift, the linear phase shift has to be negative, which requires in general anomalous dispersion of the medium (dispersion is described in more details in section 3.3.2). To achieve phase-matching the relation between power levels, propagation constants and frequencies is essential.

The efficiency of energy transfer between pump, signal and idler when the frequency separation between pump and signal is increased depends on the dispersion properties of the $\chi^{(3)}$-medium. This behavior can be summarized with the conversion bandwidth Ω_{FWM}. The conversion bandwidth is defined as the signal-pump frequency separation at which the signal gain decreases by around 3-dB and is given by [16]

$$\Omega_{\mathrm{FWM}} \approx \left[\frac{4\pi}{\beta_2 z}\right]^{\frac{1}{2}}, \tag{2.15}$$

where β_2 is the group-velocity dispersion (GVD).

With either low GVD or short interaction length z, the conversion bandwidth can be increased. One huge advantage of integrated optical systems is the potential for strong light confinement that results in very good feasibility to tailor the dispersion properties. In combination with the short length of these systems, it is possible to achieve a very large conversion bandwidth. To give an example, by dispersion engineering of the waveguide, broadband wavelength conversion over $\sim$200 nm has been shown in an integrated silicon waveguide [16].

Chapter 3

Waveguide theory

Integrated optical systems offer the opportunity to tailor the dispersion and achieve high confinement in small structures, therefore achieving high optical intensities at moderate power levels. These are ideal conditions for realizing nonlinear optics with high efficiency and over broad bandwidth. In this chapter wave guiding structures and their basic physical properties are introduced.

3.1 Confined-wave propagation

The propagation of an optical beam in free space or bulk media is accompanied by the phenomenon of diffraction. This phenomenon describes the spatial broadening of optical radiation upon propagation. In order to avoid the divergence associated to this effect and guide light in a confined manner over distance, waveguiding structures are designed and manufactured. Waveguides are composed of mainly two distinct regions, a core medium enclosed by a cladding. The two areas are distinguished by a refractive index difference where the core displays a higher refractive index than the surrounding cladding. Crucial for wave guiding is the behavior of light at the interface of the two regions. The confinement upon propagation can be understood from a ray-optics picture, where the energy of the wave confined in the core experiences total internal reflection at the interface with the cladding [32]. The propagation of light in a waveguide is described by the wave equation

$$\nabla^2 \mathbf{E} - \frac{1}{c^2}\frac{\partial^2 \mathbf{E}}{\partial t^2} = -\mu_0 \frac{\partial^2 \mathbf{P}_L}{\partial t^2} - \mu_0 \frac{\partial^2 \mathbf{P}_{NL}}{\partial t^2}. \tag{3.1}$$

The wave equation is derived from Maxwell's equations. The electric field and the material polarization are given by $\mathbf{E}$ and $\mathbf{P}$, the speed of light in vacuum is c and the vacuum permeability is μ_0. The Nabla-operator ∇ represents the differential operation $(\frac{\partial}{\partial x}, \frac{\partial}{\partial y}, \frac{\partial}{\partial z})$ for the spatial directions x, y and z.

3.2 Waveguide designs

The light guiding by total internal reflection requires a refractive index difference between the core and cladding materials. In order to achieve this index contrast, the proper materials have to be chosen. Several different platforms provide the required refractive index features, and various different waveguide designs have been developed that offer confined light propagation. One important design, essential for the success of optical communication, is the optical fiber where core and cladding are circular rods presented in Fig. 3.1.a. In the figure, z indicates the propagation direction of the optical wave. The material of choice for typical optical fibers is fused silica with slightly different compo-

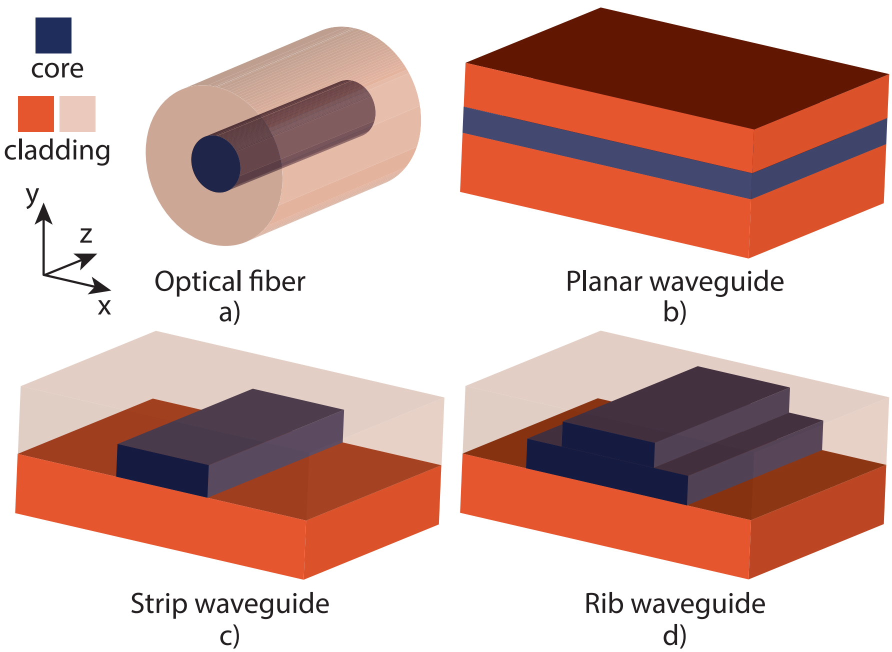

Figure 3.1: Schematics of basic waveguiding geometries. a) Optical fiber. b) Planar waveguide. c) Strip waveguide. d) Rib waveguide.

sition of core and cladding. The refractive index difference is only around 0.01 and a common core diameter of a standard single-mode fiber (SSMF) used for telecommunication is around 10 μm.
It is important to distinguish the fiber design from designs suitable for integration in micro- and nanoprocessing facilities. As fibers are drawn from a seed with proper core-cladding composition, the cylindrical design form is favorable. In contrast to this, integrated waveguide designs are based on planar layer deposition and structuring. Suitable basic designs for the integration are presented in the following. A fundamental waveguide that is the base for elementary calculations of the electromagnetic field in the structure is the planar waveguide shown Fig. 3.1.b. This is the simplest design for integrated waveguides as it consists of three unprocessed stacked layers. The index difference between core and cladding allows light confinement in the vertical direction, but confinement in the horizontal direction can not be achieved in this design. To confine the light in the transverse and lateral direction, the core medium has to be surrounded by cladding material in both x- and y-direction. The strip waveguide design illustrated in Fig. 3.1.c enables this. Width and height of the waveguide can be varied in the manufacturing process. For this design one etching step is required in order to pattern the core in the horizontal direction. With the strip waveguides it is possible to achieve waveguide bends allowing the routing of light on chip and the design of more advanced photonic systems. Another popular waveguide design for confinement in x- and y-direction is the rib waveguide shown in Fig. 3.1.d. In comparison to the strip waveguide this design requires two etching steps. This design is used for modulators where the material of the waveguide's sides is changed to apply an electrical field in order to modulate the light in the waveguide with an electro-optic effect. The waveguide designs of both Paper A and Paper B are strip waveguides.

3.3 Mode properties

3.3.1 Mode field

As light propagates in a waveguide, only specific transverse field distributions of the electromagnetic field can be propagated. These field distributions are termed the modes of the waveguide. Information about the modes is achieved by solving the wave equations (Eq. 3.1) for the concrete combination of waveguide design and material distribution. Only a few structures, such as the cylindrical geometry and the slab waveguide allow for an analytical treatment. Otherwise, this equation needs to be solved numerically given the boundary conditions and specific material information. Depending on the optical wavelength, the waveguide dimensions and the used materials, the number of modes in the waveguide varies. If only the fundamental mode propagates, the waveguide is called single mode. In order to simplify matters, a solution of the wave equation is approximated with a uniform plane wave propagating in z direction as given by

$$E(x, y, z) = E(x, y)\exp(i\beta z). \tag{3.2}$$

Here $E(x, y)$ represents the spatial field distribution transverse to the propagation direction and β indicates the propagation constant of the mode. Both parameters are characteristic for the mode and describe the propagation of the electromagnetic field completely. For simplification, only the time-independent factor of the electrical field, the complex amplitude $E(x, y, z)$, is shown by utilizing the slowly varying envelope approximation.

How well the optical field is confined inside the core area is described by the effective area parameter [28]

$$A_{\text{eff}} = \frac{\left(\int\limits_{-\infty}^{\infty}\int\limits_{-\infty}^{\infty} |E(x,y)|^2 \, dxdy\right)^2}{\left(\int\limits_{-\infty}^{\infty}\int\limits_{-\infty}^{\infty} |E(x,y)|^4 \, dxdy\right)}. \tag{3.3}$$

As can be seen in the equation, the field distribution $E(x, y)$ is important to calculate the effective area. The modal field distribution is dictated by the waveguide design and the index contrast between the core and the cladding. In general, higher-order modes and longer wavelengths result in larger effective areas. As a comparison, a typical SSMF has an effective area of around 100 μm^2, whereas in a silicon strip waveguide an effective area of 0.054 μm^2 has been presented with an air cover to increase the core-cladding index contrast [33]. For high-density integrated photonics with waveguides of short bending radii ($\leq 10\mu m$) a high optical confinement is essential.

3.3.2 Dispersion

The propagation of light in bulk media is affected by the refractive index n_0 of the medium. The dependence of the refractive index on the wavelength is well known as chromatic dispersion of the material. From an integrated optics point of view it is interesting to mention that the optical phase shift of light in waveguides can be different from the one occurring in bulk media. This is accounted for by introducing the effective index n_{eff} as

$$n_{\text{eff}} = \frac{\beta}{k_0}, \tag{3.4}$$

where $k_0 = \frac{2\pi}{\lambda_0}$ is the wavenumber with λ_0 as the wavelength in vacuum. Different modes and modes at different polarization have a different effective index n_{eff}. The effective index accounts for the influence of core and cladding materials and the waveguide design. The effective index of a guided mode has a value in between the refractive index of the cladding n_{cl} and the core n_{cl} materials given by $n_{\text{cl}} \leq n_{\text{eff}} \leq n_{\text{co}}$. As n_{eff} is wavelength dependent, the material dispersion is supplemented by a waveguide contribution to the total dispersion. More detailed information about the wavelength dependent phase shift in the waveguide is revealed when writing β as a Taylor expansion around a center frequency ω_0 given by [28]

$$\beta(\omega) = \beta_0 + \beta_1(\omega - \omega_0) + \frac{1}{2}\beta_2(\omega - \omega_0)^2 + \ldots \quad . \tag{3.5}$$

The individual β_m account for different contributions to the propagation constant and are calculated by

$$\beta_m = \left(\frac{d^m \beta}{d\omega^m}\right)_{\omega=\omega_0} . \tag{3.6}$$

The parameter β_0 is connected to the phase velocity of a monochromatic wave by $v_p = \frac{\omega_0}{\beta_0}$. The group velocity of a pulse envelope is related to β_1 by $v_g = 1/\beta_1$. Information about how a pulse is affected by temporal broadening during propagation is connected to the amount and sign of the group-velocity dispersion (GVD) β_2. The broadening comes from the different propagation speeds of the individual frequency components forming a pulse. One distinguishes between normal dispersion with a positive GVD ($\beta_2 > 0$) and anomalous dispersion with a negative GVD ($\beta_2 < 0$). In the anomalous dispersion regime the higher frequency (blue-shifted) components propagate faster than the lower frequency (red-shifted) components of an optical pulse and vice versa. The value of the GVD is important for phase-matching in nonlinear optics (as explained in sec. 2.4). It is highly relevant to re-emphasize that for high confinement waveguides the GVD depends on the waveguide parameters, and the dispersion can be tailored e.g. by changing the dimensions of the waveguide. In Paper B simulations were presented, that show the dependence of the waveguide dimensions of a strip waveguide on the GVD. It is common to describe the GVD with the dispersion parameter D where the group velocity is in relation to the wavelength given by

$$D = \frac{d\beta_1}{d\lambda} = -\frac{2\pi c}{\lambda^2}\beta_2 \tag{3.7}$$

and typically expressed in [ps/(nm·km)].

3.3.3 Polarization

The electromagnetic wave description assigns a direction of oscillation to the electric and magnetic field component as it propagates in time and space. In

isotropic media the propagation behavior, more precisely the refractive index the wave experiences, is independent on the electromagnetic field oscillation. However, in anisotropic media the refractive index is dependent on the orientation of the electric field, leading to effects like polarization-mode dispersion. It is common to define the electric field as the superposition of two polarization states, the TE and the TM polarization modes. For the TE polarization the electrical field component in propagation direction is zero and for TM polarization the magnetic field component in propagation direction is zero [34].
Although the materials forming a waveguide are mostly isotropic, the waveguide itself can however show anisotropic optical properties. This can be the case in rectangular waveguides. As the field components in propagation direction are only close to zero, one talks about hybrid modes, in particular quasi-TE and quasi-TM modes. In addition, for structures with a small refractive index difference between core and cladding, the two polarization states (quasi-TE and quasi-TM) have dominant electrical field components either in horizontal x-direction or vertical y-direction labeled by E^x_{pq} and E^y_{pq}, where p relates to the mode-order in x-direction and q relates to the mode-order in y-direction. In order to exemplify the difference of the effective index in dependence of the mode-order and polarization, the modes that are present in an integrated strip waveguide with typical dimension of 1000 nm in width and 500 nm in height are compared in Fig. 3.2. A mode-solver was used to calculate the modes. The simulations were carried out using COMSOL Multiphysics where Maxwell's equations are solved using the finite element method. The waveguide, here silicon nitride as the core material and silicon dioxide as the cladding material, has two guided modes for both states of polarization at 1550 nm wavelength. The figure shows the power distribution in propagation direction and it can be seen that the effective index changes with state of polarization and mode-order. In applications, the birefringent dependence of the waveguide design has been utilized to build integrated photonic systems like polarization rotators and polarization splitter [35, 36], as well as polarizers [37]. Even polarization independent designs have been demonstrated [38].

3.4 Loss mechanisms

3.4.1 Propagation loss

The propagation loss in integrated optical waveguides has three fundamental linear contributions which are material absorption, scattering loss and radiation loss [39]. All loss contributions are summarized in the loss parameter α

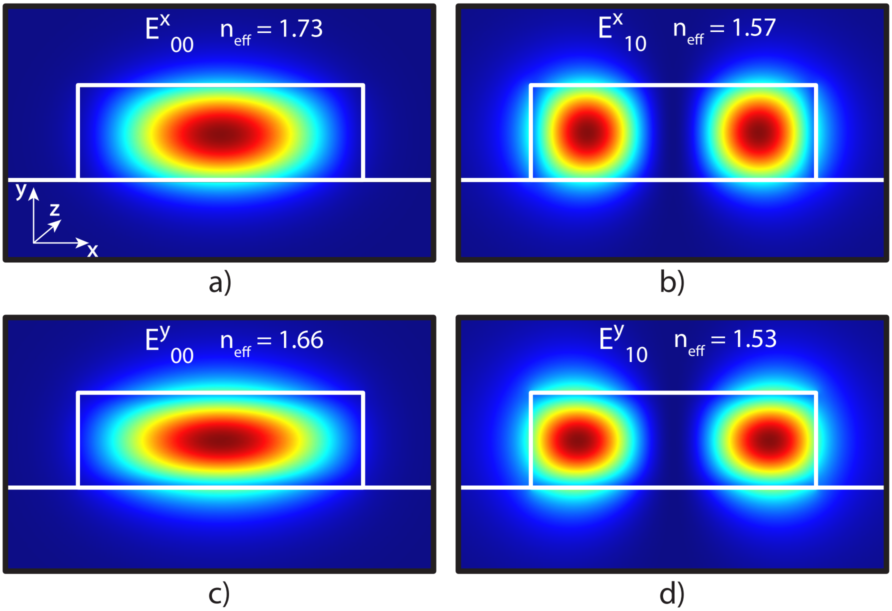

Figure 3.2: Mode-solver simulations of the power distribution in propagation direction z for a strip waveguide with dimensions of 1000 nm in width and 500 nm in height. The core and cladding materials are silicon nitride and silicon dioxide. a) Fundamental quasi TE-mode (E^x_{00}). b) Second-order quasi TE-mode (E^x_{10}). c) Fundamental quasi TM-mode (E^y_{00}). d) Second-order quasi TM-mode (E^y_{10}).

that leads to an exponential power decay along propagation distance z according to

$$P = P_0 \exp(-\alpha z), \tag{3.8}$$

where P_0 is the initial power before propagation. In nonlinear optics, the propagation loss plays a significant role. In calculations of nonlinear processes the total physical length of the waveguide L is commonly replaced by the effective length L_{eff} given by

$$L_{\text{eff}} \equiv \frac{1 - \exp(-\alpha_{\text{lin}} L)}{\alpha_{\text{lin}}}, \tag{3.9}$$

where α is the linear attenuation coefficient[1]. The effective length represents the waveguide length before the power attenuation becomes significant.

[1]The conversion from attenuation in dB/m to linear attenuation is given by the relation $\alpha = 4.343 \cdot \alpha_{\text{lin}}$.

The origin of material absorption lies in the interaction of optical waves with the medium during propagation. This interaction leads to energy transfer from the wave to the material that can be elastic or inelastic. In the case of an inelastic process, the energy of the wave is not conserved but transferred to the medium. This effect causes propagation loss by material absorption. The absorption loss is characterized by its frequency dependence as different frequencies interact in diverse manners with the charges and bonds present in matter resulting in material specific transparency windows. Impurities in the material can lead to additional absorption. A known example for a molecular-bond-related absorption wavelength is the oxygen-hydrogen bond (O-H) whose oscillation behavior absorbs light around telecom wavelengths.
Another contribution to the propagation loss is the scattering loss that occurs at the interfaces between core medium and cladding medium. The surface roughness of the core surfaces due to fabrication imperfections in the deposition and etching processes leads to scattering of light. The amount of scattering loss is related to the mean value of the roughness at the surface and its statistical variance [40]. The confinement of light and thus the interaction with the sidewall changes with core-cladding index contrast, mode order, wavelength and polarization. Waveguides with very thin sidewalls of only 40-50 nm lead to record low propagation loss [22]. A similar core thickness has been used in the work of Paper A. In Paper B the roughness of the waveguide sidewalls and top surface has been analyzed in order to characterize the scattering loss. Another origin of scattering loss are imperfections in the core material, but this effect is rather small compared to surface scattering loss.
The third contribution to propagation loss, the radiation loss, becomes relevant when waveguides are bent. In a curved waveguide the optical field is distorted in comparison to a straight waveguide which can lead to radiation of optical energy into radiating modes. The radiation loss becomes larger for shorter bending radii and waveguides with lower light confinement [41]. Therefore, in integrated optical systems the minimum achievable bending radius is mainly limited by radiation loss rather than by processing tolerances [39].

3.4.2 Nonlinear loss

In the field of nonlinear optics when working with highly confined optical fields at high power levels, nonlinear loss contributions become relevant in certain materials. In the presence of nonlinear loss, the total loss coefficient changes to

$$\widetilde{\alpha} = \alpha_{\mathrm{L}} + \alpha_{\mathrm{NL}}(|E|^2), \tag{3.10}$$

where α_{L} describes the linear contribution to the loss and α_{NL} accounts for nonlinear loss. Examples of nonlinear loss is interband absorption like two-photon absorption (TPA) that occurs in materials for integrated optics like silicon or chalcogenide glasses (ChGs) at telecommunication wavelengths [18, 42]. During the TPA process the energy of two photons is absorbed in order to bridge the band-gap energy and excite electrons from the valence band to the conduction band. This nonlinear loss has intensity dependence according to

$$\alpha_{\mathrm{NL(TPA)}} = \alpha_2 \left|E\right|^2 , \tag{3.11}$$

where α_2 is the TPA absorption coefficient. The free carriers generated by TPA give rise to another nonlinear loss mechanism, the free carrier absorption (FCA). In this process photon energy is transferred to free carriers in the conduction band or holes in the valence band. The emerging nonlinear loss is proportional to the free carrier concentration [39]. A possible way to counteract the FCA is the removal of free carriers from the waveguide region, this has been shown in devices based on a reverse biased p-i-n structure in rib waveguides [43].

3.4.3 Coupling loss

The coupling of light from an optical fiber to an integrated waveguide is commonly done by the direct focusing (end-fire) approach or by grating couplers. In the end-fire coupling approach light is focused directly from the fiber to the bare integrated waveguide. The coupling efficiency is dependent on the overlap integral of the field of the incident beam and the mode field of the waveguide and is calculated by [39]

$$\eta_m = \frac{\left(\int A(x) B_m^*(x) dx\right)^2}{\int A(x) A^*(x) dx \int B_m(x) B_m^*(x) dx}. \tag{3.12}$$

To simplify the equation only the transverse direction is considered where $A(x)$ and $B_m(x)$ are the field distributions of the incident beam and the m-th mode of the waveguide. The equation shows that improved coupling is achieved for matching the two mode field $A(x)$ and $B_m(x)$.
Spot size converters at the end of the waveguides are commonly used to tailor the mode field in the integrated system to match the one of the incident beam in order to increase coupling efficiency. In [44] a coupling loss of 0.2 dB per facet has been demonstrated using a spot size converter.
Grating couplers are periodic grating structures that allow coupling of light from an oblique angle to the direction of the waveguide [45]. The advantage of grating couplers in comparison to end-fire coupling is that cleaving of the wafer is not needed, thus making on wafer testing possible. A drawback is the limited bandwidth and polarization dependence. In [46] a grating coupler design

with a coupling loss of 0.62 dB and a 1-dB bandwidth of 40 nm has been shown.

3.5 Nonlinear coefficient

It is convenient to summarize the nonlinear behavior of an integrated waveguide in the nonlinear coefficient γ as given in

$$\gamma = \frac{2\pi n_2}{\lambda A_{\text{eff}}}, \tag{3.13}$$

where n_2 is the Kerr coefficient of the material, λ is the wavelength and A_{eff} is the effective area. The equation shows that both the nonlinear Kerr properties of the material and the field confinement have significant contributions to an increased γ. The confinement of the light defines the intensity of light for a given power. With a given nonlinear coefficient γ, power P and effective length L_{eff}, the maximum nonlinear phase shift in a waveguide is

$$\theta_{\text{NL}} = \gamma P L_{\text{eff}}. \tag{3.14}$$

In an example the maximum nonlinear phase shift in a silicon waveguide is calculated. Considering the following reasonable parameters $\gamma = 100\ (\text{W}\cdot\text{m})^{-1}$, $P = 100$ mW, $L = 3$ cm, $\alpha = 2$ dB/cm a nonlinear phase shift of $\theta_{\text{NL}} = 0.3$ rad is achieved.

Chapter 4

Materials for integrated nonlinear optics

Research based on nonlinear optical phenomena has been carried out in the last decades in several distinct material compositions. In this chapter we present and compare material platforms that are established in the field of integrated nonlinear optics. The presented materials are categorized into three different groups: Chalcogenides, III-V materials and CMOS-compatible materials. In the following the three groups are presented in terms of linear and nonlinear optical properties and afterwards compared to one of the most common widespread solution, i.e. a highly nonlinear fiber (HNLF) of silicon-doped glass commercially available.

4.1 Chalcogenides

The family of chalcogenide glasses (ChGs) is based on the chalcogen elements from group VIa of the periodic table presented in Fig.4.1 [42]. In particular the element sulphur, selenium and tellurium form glass compounds with elements like phosphorous, germanium or arsenic. To form the glass compounds, deposition techniques like thermal evaporation, sputtering or chemical vapor deposition (CVD) can be used, followed by a post-deposition annealing step. ChGs are amorphous semiconductors and by tailoring the atomic composition of the glasses the optical properties can be changed. For instance the transparency of the ChGs is affected by the used chalcogen element, and the transparency window enters into the mid-infrared region (sulphides 11 μm, selenides 15 μm, tellurides 20 μm) [42]. With a linear refractive index of $\sim 2-3$ at 1.55 μm, these glasses can be integrated as an optical waveguide core medium with different surrounding cladding materials, such as SiO_2.

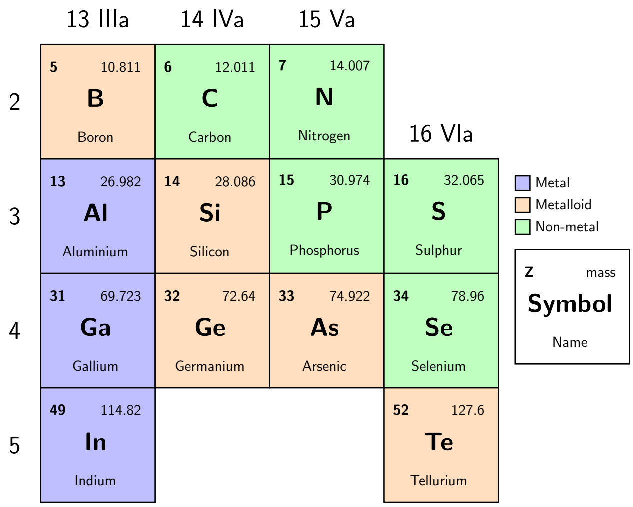

Figure 4.1: Selected section of the periodic table with relevant materials for integrated nonlinear optics.

Examples for ChGs are the selenium based compound GeAsSe and the sulphur based compound As_2S_3. The glass GeAsSe has very high Kerr nonlinearities of up to $0.9{\cdot}10^{-17}m^2/W$ with a very low two-photon absorption (TPA) coefficient [47, 48]. Waveguides created with this material have been used to demonstrate FWM and supercontinuum generation [47]. A more common chalcogenide material in the field on integrated nonlinear optics is As_2S_3. Although it has a three times lower Kerr coefficient than GeAsSe, the lower waveguide losses achieved while having similar low TPA make it the more suitable ChGs for applications in the telecommunication band [49]. Using rib waveguides made from As_2S_3, several nonlinear applications have been shown, like FWM [50, 51] and wavelength conversion based on XPM [52] and FWM [53]. Also supercontinuum generation [49] and SPM assisted signal regeneration [54] has been shown.

4.2 III-V materials

The group of III-V materials is based on compounds formed between elements from group IIIa (aluminum, gallium or indium) and group Va (nitrogen, phosphorous, arsenic) in the periodic table shown in Fig.4.1. Due to the direct bandgap in III-V materials they are commonly used in amplifiers (semiconductor optical amplifiers (SOAs)) or light emitting devices, including lasers. The

crystalline semiconductor materials are mainly grown by molecular beam epitaxy (MBE) or metalorganic chemical vapor deposition (MOCVD) in order to achieve layer by layer growth of crystalline morphology. This epitaxial growth requires a crystalline substrate and misses flexibility of stacked deposition on top of non-crystalline materials. Using III-V materials in CMOS-process lines is strictly avoided due to contamination of the fabrication line as III-V elements serve as dopants for silicon.
III-V materials like GaAs or AlGaAs are transparent through the communication bands and are utilized for nonlinear integrated optics. As the materials form compounds, the optical properties can be varied by changing the atomic composition of the compound. For instance, both the refractive index and bandgap increases by adding aluminum to GaAs, hence becoming AlGaAs. The nonlinear coefficient of these materials is very high with $1.6 \cdot 10^{-17}\mathrm{m}^2/\mathrm{W}$ for GaAs [55] and even $2.6 \cdot 10^{-17}\mathrm{m}^2/\mathrm{W}$ for AlGaAs [56]. However, in the compound of GaAs, large nonlinear loss $\sim 100 \cdot 10^{-13}\mathrm{m}/\mathrm{W}$ [19] limits the launched power levels. A significant reduction of nonlinear loss by more than one order of magnitude is achieved with increased content of aluminum in AlGaAs [57] because of the increase in bandgap. The high nonlinearities and moderate linear propagation losses lead to nonlinear experiments in AlGaAs like FWM [57, 58]. Wavelength conversion assisted by XPM has been shown in waveguides [55] as well as in resonators [59]. Even microresonator based comb generation has been shown [56]. In AlGaAs outstanding performance has been achieved by demonstrating a FWM conversion bandwidth of 750 nm [60] and a record low power threshold (7 mW) for comb generation [61].

4.3 CMOS-compatible materials

The manufacturing facilities for CMOS electronics have matured over the last decades and allow for low cost and mass production of electronic devices. Silicon, a group IV element, is the base material for CMOS components [62] but it is also attractive for nonlinear integrated optics [14] due to its large transparency window between 1 and 9 μm and its large nonlinear Kerr coefficient. A description of CMOS-compatible processing is given in more detail in the next chapter. In the field of nonlinear integrated optics, pure silicon is used both in crystalline and amorphous morphology. Silicon is also used in a compound with nitrogen (group V), forming silicon nitride, which is another CMOS-compatible material and widely used for nonlinear integrated optics.

4.3.1 Silicon

Crystalline silicon
Integrated silicon waveguides are mainly based on the commercially available

silicon-on-insulator (SOI) platform. This platform, originating from CMOS electronics, offers a single-crystalline silicon film separated by a layer of silicon dioxide from the bulk substrate. This layer combination is not possible to fabricate by deposition, but achieved by wafer bonding [63] and is most suitable for the fabrication of waveguides. Crystalline silicon offers a large Kerr coefficient of $0.4 - 0.9 \cdot 10^{-17}\mathrm{m}^2/\mathrm{W}$ [18, 19]. A high refractive index contrast is given when silicon (3.5 at 1.55 μm) is embedded in silicon dioxide (1.45 at 1.55 μm). Under this condition the light guided in the silicon core is highly confined which leads to high optical intensities. The drawback of silicon as a material for nonlinear optics is the low optical bandgap leading to a TPA coefficient of around $50 \cdot 10^{-13}\mathrm{m}/\mathrm{W}$ in the telecommunication band [18, 19]. Upon TPA, free carriers are generated in the waveguide which causes further absorption loss and a shift in dispersion. The resulting free-carrier absorption is setting a limit to the maximum intensity level where efficient nonlinear processes are possible.
Free carriers can be removed from the waveguide core with an applied electric field [64, 65]. In order to apply the electric field, a reverse biased p-i-n diode design is used in a rib waveguide structure. Nonlinear experiments that have been presented in SOI-based silicon waveguides with and without carrier removal design include signal regeneration [15, 66], supercontinuum generation [17] and third-harmonic generation (THG) [67]. Furthermore FWM has been demonstrated in nonresonant structures [68–70] as well as in microring resonators [71, 72]. Wavelength conversion with data rates up to 40 Gb/s has been shown in [73, 74]. It is worth highlighting that in crystalline silicon the highest continuous wave (CW) FWM conversion efficiency (-1 dB) has been achieved over all platforms in waveguides using biased p-i-n diodes for carrier removal [43].

Amorphous silicon
Low-temperature deposited silicon in amorphous form has raised interest in recent years because of its increased nonlinear Kerr coefficient and reduced TPA coefficient compared to crystalline silicon. An increased Kerr coefficient in amorphous silicon compared to crystalline silicon is explained by the existence of midgap localized states that furthermore leads to reduced nonlinear TPA [75]. The deposition in a plasma-enhanced chemical vapor deposition (PECVD) step (further information in 5.4.2) allows process temperatures as low as 200-400 °C. The possibility of deposition, that is not given for crystalline silicon, allows the fabrication of multiple layer designs and possible vertical coupling between waveguides. Deposited amorphous silicon has dangling bonds[1] that are commonly saturated with hydrogen leading to hydrogenated

[1] Dangling bonds are unsaturated material bonds that have energy states withing the bandgap of the material resulting in strong absorption in the near infrared (IR) [76].

amorphous silicon (a-Si:H) suitable for integrated optics [76]. One large drawback of amorphous silicon is its temporal instability. Although material degradation can be reversed by annealing, a variation of system performance can be expected [77]. Indeed, reported nonlinear Kerr coefficients for a-Si:H vary from 0.05 to 7.43 $\cdot 10^{-17} \mathrm{m}^2/\mathrm{W}$ [78–83] indicating a large dependence of the material on the processing parameters. TPA coefficients of around 10-30 $\cdot 10^{-13} \mathrm{m/W}$ have been presented [78–81] that is roughly a factor of two below crystalline silicon. The potential for nonlinear optics has been shown in FWM experiments [80, 84] and FWM based wavelength conversion [79]. Additionally spectral broadening induced by SPM [82] and XPM [78] has been presented, as well as supercontinuum generation [85, 86].

4.3.2 Silicon nitride

Another CMOS-compatible material that is widely used to integrate nonlinear photonic systems is silicon nitride. In the CMOS fabrication process silicon nitride is used as a thermal and electrical isolator. Silicon nitride can be deposited in low-pressure chemical vapor deposition (LPCVD) and plasma-enhanced chemical vapor deposition (PECVD) process steps (details about both processes are provided in 5.4) as well as by sputtering. With these different techniques the material deposition can be performed at various temperatures giving large flexibility of fabrication. The material has in general amorphous morphology. The elementary material composition is crucial when characterizing its optical properties. In the field of nonlinear photonics three main compositions have been presented: stoichiometric silicon nitride Si_3N_4 (Paper A); silicon rich nitride with non-stoichiometric composition Si_xN_y (Paper B); and a proprietary material named Hydex, whose properties are similar to silicon oxynitride SiO_xN_y [21].

Stoichiometric silicon nitride

Stoichiometric silicon nitride has a transparency window from 0.25 to 8 μm, and it has potential as a core material for integrated optics, including visible light applications. The refractive index of stoichiometric silicon is ~ 2 at 1.55 μm. Waveguides manufactured with Si_3N_4 and SiO_2 as core and cladding materials show low propagation losses and good optical confinement allowing for high intensity optics with long interaction lengths. Among all the presented materials, this material platform provides waveguides with the lowest propagation loss of 0.001 dB/cm [22] and ring resonators with the highest Q-factors ($\sim$80 million) [87]. The large bandgap of Si_3N_4 in the order of 5.3 eV [88] allows neglecting TPA in the telecommunication band. This, together with the low propagation loss, is the base for high intensity nonlinear optics that can not be achieved in silicon. The nonlinear Kerr coefficient however is around 2

$\cdot 10^{-19}$m^2/W [23], roughly two orders of magnitude lower than silicon.
One main fabrication challenge when depositing thick layers of Si_3N_4 is an increased tensile stress in the film that leads to cracking of the layer above ∼250 nm [89]. A large thickness is required for optimal dispersion engineering and high light confinement. To overcome this challenge strategies have been investigated including thermal cycling [90], PECVD frequency alternation [91], mechanical stress barriers [26] and deposition in trenches [92]. With thin waveguides (40-50 nm) the cracking problem is avoided completely and in addition ultra-low propagation loss properties are achieved by reducing the sidewall scattering losses [22]. In thick high-confinement waveguides, the nonlinear capability of this material has been shown in experiments like supercontinuum generation [93], harmonic generation in a microring cavity (second-harmonic generation (SHG) and third-harmonic generation (THG))[94] and resonator based Kerr frequency comb generation [90, 95–97]. In thin waveguides with very low propagation loss FWM-based wavelength conversion has been demonstrated in Paper A. Over all presented platforms the broadest supercontinuum generation (495 THz) has been achieved in stoichiometric silicon nitride presented in [25].

Silicon-rich nitride
The variation of the ratio of silicon and nitrogen in non-stoichiometric silicon nitride, Si_xN_y, gives a degree of freedom to change the optical and mechanical properties of the material. This enables for instance tuning the refractive index between the one achieved for Si_3N_4 and amorphous silicon as shown in [98]. Silicon nitride with an increasing content of silicon is often referred to as silicon-rich nitride. Flexible deposition with variable composition of Si_xN_y is given within the CMOS fabrication environment. This material[2] has with 1.4 $\cdot 10^{-18}$m^2/W a 5 times higher Kerr coefficient than Si_3N_4 as shown in Paper B. A higher refractive index of around 2.1 (at 1.55 μm) (Paper B) than Si_3N_4 leads to higher light confinement in the waveguide. Furthermore, a relaxation of the tensile stress is achieved when growing these layers [27, 99], allowing to achieve thick cores in a single deposition step. These advantages of increased silicon content come with a reduced bandgap that can give rise to increased TPA effects. The nonlinear performance has been presented in a FWM experiment in Paper B.

Hydex
Hydex, invented by the company Little Optics, is a high-index doped silica glass with a refractive index between 1.5 and 1.9 (at 1.55 μm) close to silicon oxynitride. It has a nonlinear Kerr coefficient of 1.1 $\cdot 10^{-19}$m^2/W [100] which is slightly below the one of Si_3N_4. Waveguides with a very low propagation loss

[2]For an atomic composition of 65% silicon to 35% nitrogen, in this case.

have been fabricated in this platform, which enables a long effective length. Nonlinear experiments have been performed in order to show the potential of Hydex waveguides for nonlinear optics including FWM [101], wavelength conversion in non-resonant waveguides [102] and resonating microrings [103] as well as supercontinuum [100] and comb generation [104, 105].

4.4 Comparison and benchmarking with HNLF

In order to compare the presented platforms used for nonlinear integrated optics, the maximum achievable nonlinear phase shift $\theta_{\mathrm{NL}} = \gamma P L_{\mathrm{eff}}$ (see section 3.5) is calculated and benchmarked with a HNLF. At the moment HNLF is the best platform for nonlinear optics in terms of maximum nonlinear phase shift. For each platform representative waveguide systems are chosen. Crucial for the calculation of the maximum nonlinear phase shift is the maximum possible launched power. Limitations are given by nonlinear loss from TPA in the case of integrated platforms, wheras in HNLF stimulated Brillouin scattering (SBS) limits the launched power. For platforms that do not show TPA a reasonable maximum launched power of 2 W is taken and for HNLF a SBS limited maximum power of 200 mW is assumed. The SBS threshold can be increased by modulating the CW pump, but this comes with a degradation in performance in some relevant experiments, for instance in optical communication applications. For platforms that are restricted by TPA the maximum launched power was chosen as the value when the nonlinear TPA loss reaches either 10% (Fig. 4.2.a) or 1% (Fig. 4.2.b) of the linear loss according to Eq. 3.11. Fig. 4.2.a shows the higher nonlinear phase shift for chalcogenides, III-V, amorphous silicon and HNLF. Crystalline silicon and silicon nitrides show a similar performance. For a more stringent demand in the maximum launched power when nonlinear loss reaches 1% of linear loss, the result changes and is presented in Fig. 4.2.b. Still ChGs, AlGaAs and HNLF show the largest nonlinear phase shift. Under this condition the material suffering from TPA shows worse performance. Silicon nitride becomes better in comparison to silicon and the best CMOS-compatible platform for nonlinear optics. The calculations of the nonlinear phase shift is based on the detailed information shown in Table 4.1.

4.5 Conclusion

It becomes clear after the presentation and comparison of the material platforms in this chapter, that there is no platform that combines all the different advantages mentioned above. In distinct platforms different record perfor-

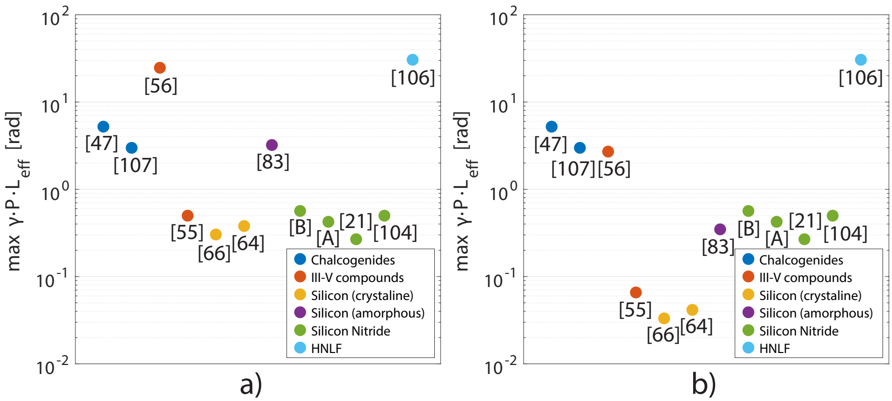

Figure 4.2: (a) Maximum nonlinear phase shift with nonlinear loss restricted to 10% of linear loss. (b) Maximum nonlinear phase shift with nonlinear loss restricted to 1% of linear loss.

mances have been achieved, which indicates that each platform can outpace each other in terms of selected features. To conclude this chapter, the major advantages and disadvantages of each material platform are briefly summarized. Chalcogenides offer good nonlinear performance and with the deposition by evaporation a fairly substrate independent deposition technique. However, the chalcogenide glasses are not CMOS-compatible.
III-V compounds have demonstrated flexibility when it comes to tailoring material properties. Especially AlGaAs unites high refractive index and high nonlinearities leading to highly efficient nonlinear processes. Missing CMOS-compatibility and the required epitaxial growth brings fabrication disadvantages.
Crystalline silicon has high nonlinearities and is a highly mature (CMOS-compatible) fabrication platform with easy access through commercially available SOI-wafers or multi-project wafer runs. Nevertheless, crystalline silicon shows nonlinear loss constraints limiting the used power levels and silicon can not be deposited in crystalline form on top of amorphous wafer substrates like silica.
Amorphous silicon shows high nonlinear Kerr coefficients and the low temperature deposition technique allows for flexible deposition with potential layer stacking. Reported temporal instability is the drawback.
Silicon-rich nitride offers CMOS-compatibility and has the possibility to be deposited flexibly on amorphous substrates. Furthermore low propagation losses are reported within this platform. The moderate nonlinearities and the high tensile stress in thick films are the drawback.

Nonstoichiometric silicon nitride is a CMOS-compatible material and offers flexible processing of thick layers suitable for dispersion engineering. The optical properties of the compound can be engineered by changing the composition of silicon and nitrogen. Propagation losses are drawbacks.
Hydex has very low propagation losses. The low nonlinearities and the low refractive index are drawbacks. The platform is not widely available

Table 4.1: Comparison of material platforms for nonlinear optics regarding the Kerr coefficient n_2, two-photon absporption TPA, effective area A_{eff}, nonlinear parameter γ, propagation loss, group-velovity dispersion (GVD) β_2 and waveguide design.

Platform	Material	n_2 $[10^{-20} m^2/W]$	TPA α_2 $[10^{-15} m/W]$	A_{eff} $[\mu m^2]$	γ $[(W \cdot km)^{-1}]$	Loss [dB/m]	GVD β_2 $[ps^2/m]$	design	ref.
HNLF	SiO_2 based	2.6	-	9	11.7	0.00086	zero-GVD at 1541 nm	fiber	[106]
ChGs	$Ge_{11.5}As_{24}Se_{64.5}$	860	6.2	0.24	136 000	250	-84	strip	[47]
	As_2S_3	300	6.2	7.10	1 700	5	433	rib	[107]
III-V	GaAs	1 590	10 000	1.80	36 000	600	n.i.[b]	strip	[55]
	$Al_{0.17}Ga_{0.83}As$	2 600	300-500	0.16	658 700	140	-127	strip	[56]
CMOS-	c-Si (with p-i-n)	500	5 000	0.058	280 000	100	n.i.[b]	rib	[66]
compatible	c-Si	400	5 000	0.006	355 600	360	-3445	strip	[64]
materials	a-Si:H	2 100	2 500	0.07	1 200 000	45	-0.42	strip	[83]
	Si_xN_y	140	-	0.90	6 300	150	-77	strip	Paper B
	Si_3N_4 (low conf.)	9 [a]	-	1.28	285	6	0.7	strip	Paper A
	Si_3N_4 (high conf.)	26	-	0.88	1 200	40	zero-GVD at 1560 nm	strip	[21]
	Hydex	11	-	2.0	220	4	10	strip	[104]

[a] effective n_2 for low-confinement waveguide
[b] no information available in reference

Chapter 5

CMOS-compatible micro- and nanofabrication

To understand the manufacturing process that enables silicon based integrated optical systems, in this chapter relevant CMOS-compatible micro- and nanofabrication steps are introduced.

5.1 CMOS-compatible photonics

Electronic components, such as microprocessors, evolved tremendously in performance during the last decades, while keeping price low and even reducing footprint size. The reasons for this can be found in the development of the micro- and nanofabrication techniques and infrastructure for electronics. Mass production and miniaturization led to a tremendous improvement of integrating functionalities on microchips referred to as integrated circuits (ICs). One key component for integrated logic is the metal-oxide-semiconductor field-effect transistor (MOSFET) which forms the building block for CMOS technology. In general, the term CMOS-compatible defines fabrication techniques and materials that may be used in a CMOS processing line without risk of contamination or other adverse effects. Materials that are compatible with the CMOS fabrication infrastructure benefit from a mature processing platform that offers ideal conditions for low-cost mass production.
The CMOS fabrication infrastructure can be leveraged to manufacture optical waveguides. With the first silicon based optical waveguide [10] the path of silicon photonics has begun to be driven by the CMOS fabrication capabilities [108, 109]. The integration of silicon photonics enables major advantages in communication systems [110]. With modern multi-project wafer runs, the high

volume processing of CMOS fabs is leveraged to give fairly low-cost access to integrated photonic systems [13, 111].

5.2 Optical lithography

One of the most important manufacturing steps in the environment of semiconductor fabrication is the lithography process. This step combines the reproducible transfer of patterns for dedicated functionality onto the wafer. The patterns are geometries dedicated to produce structures as e.g. electrical contacts, passivation areas, areas for localized doping or etching of ridges, trenches or mesas. It is important to mention that during the lithography step the geometries are only structured and prepared for further processing steps such as etching. Optical lithography offers high throughput and comes with relatively affordable equipment.

In the lithography process the system design is projected via a photomask onto a photosensitive polymer on the wafer. The photomask contains transparent parts (glass) and opaque parts (chromium). As the photomask is aligned in between the light source and wafer (with photoresist), the optical radiation passes through the photomask and exposes only the selected areas of the resist where the photomask is transparent. The photosensitive resist then undergoes a chemical change when exposed to radiation. An example of the exposure step during the lithography process is illustrated in Fig. 5.1.a. Light sources used for optical lithography are in the regime of ultraviolet (UV), deep ultraviolet (DUV) or extreme ultraviolet (EUV), reaching wavelengths from 400 nm down to around 100 nm. The resolution in terms of the minimum feature size that can be exposed scales with wavelength. In the case of optical contact lithography where photomask and wafer are in contact, the minimum resolved features are described by [62]

$$W_{min} \approx \sqrt{k\lambda g}, \tag{5.1}$$

where λ is the wavelength, k is the resist specific technology parameter (often around 1) and g is the gap between photomask and wafer. As an example, a gap of 2 μm and a light source with 300 nm wavelength would give a minimum feature size of around 800 nm. In the case of projection lithography the minimal feature size is described by [62]

$$W_{min} \approx k\frac{\lambda}{\mathrm{NA}}. \tag{5.2}$$

Here an objective with a numerical aperture (NA) is placed between the mask and wafer in order to project a smaller image of the mask onto the wafer and achieve a scaling down of the mask geometries. Both equations show

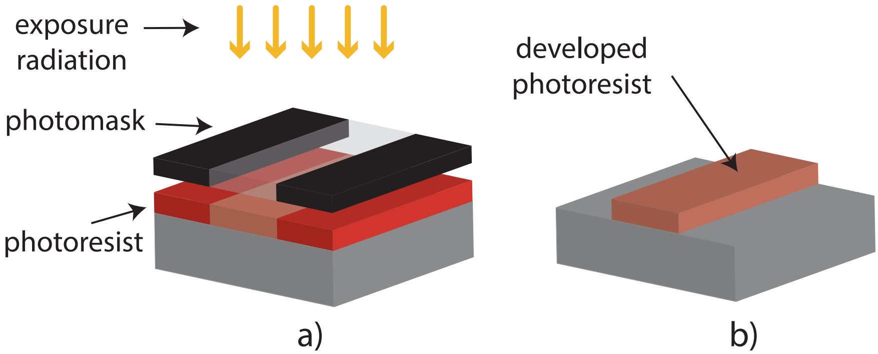

Figure 5.1: Illustration of optical lithography a) Illustration of the exposure process. The dark areas of the photomask are opaque. The bright area of the photomask is transparent for the exposure radiation. b) Illustration of the developed positive photoresist after exposure.

that lithography using shorter wavelengths means a smaller minimum feature size that can be resolved during exposition. After exposure the photoresist is developed where exposed parts are removed for positive photoresists, while unexposed parts are removed for negative photoresists. The exposing radiation activates a different photosensitive chemistry in positive and negative resists. In positive resist the radiation triggers a scission of polymer chains leading to the reduction of its molecular weight that makes it easier to be resolved during development. The opposite effect takes place in a negative resist where cross polymerization leads to a reduced dissolution behavior. The remaining resist structures can serve as an etchmask or define openings for other processing steps like metal deposition with lift-off. The developed positive photoresist of the lithography example is illustrated in Fig. 5.1.b.

A higher resolution than optical lithography can be achieved using electron-beam electron-beam (ebeam) lithography. A shorter wavelength compared to optical radiation is achieved by the acceleration of electrons to high energies. Electron-sensitive resist is exposed by a focused electron beam. This technique is used to create photomasks or write masks directly on the wafer for very small features. Although writing features of well below 100 nm [62] are possible, the ebeam lithography has a serial writing procedure making the process time consuming, and the equipment is expensive and complex. This lithography is therefore unsuitable for mass production and in that sense not CMOS compatible.

The fabrication processes developed in Paper B and A make use of optical contact lithography. In Paper B a DUV-light source with a wavelength around 220 nm was used and openings of 400 nm were resolved completely after the lithography and etching process. The usage of optical projection lithography has been reported in [41] where a light source with 193 nm wavelength was used and waveguide widths from 150 to 500 nm were achieved.

5.3 Thermal oxidation

The success of silicon as the primary semiconductor material in the field of electronics is based on its high-quality oxide [62]. A low amount of defects and an easy fabrication process makes the combination of silicon and silicon dioxide a powerful alliance in integrated circuits with fast switching MOSFETs with low power consumption. The oxide is formed during an oxidation process in which silicon undergoes a chemical reaction with oxygen in order to create silicon dioxide according to [62]

$$\mathrm{Si(solid)} + \mathrm{O_2(gas)} \longrightarrow \mathrm{SiO_2}. \tag{5.3}$$

It is important to mention that the oxidation reaction only takes place at the silicon surface. As a layer of SiO_2 builds up on top of the silicon wafer, oxygen atoms have to diffuse through the oxide layer in order to react at the silicon surface to form the SiO_2. At room temperature a silicon wafer oxidizes by only 2.5 nm and further oxidation is halted as the mobility of oxygen atoms is too low to diffuse through the oxide layer. Therefore thermal oxidation is carried out at process temperatures around 700-1200 °C for increased diffusion of oxygen towards the silicon surface. Silicon oxidation is commonly done under atmospheric pressure (760 torr) and a distinction is made between dry oxidation with molecular oxygen O_2 as oxidant and wet oxidation with water vapor H_2O as oxidant. Dry oxidation has the advantage of a denser oxide with higher quality whereas in wet oxidation a higher oxidation rate is achieved. An illustration of the wet oxidation process is presented in Fig. 5.2. The oxidation reaction is indicated by R and takes place at the interface between silicon and silicon dioxide. Gaseous water molecules have to diffuse from the wafer environment through the silicon dioxide to reach the interface. The diffusion process is marked by D. The oxidation rate becomes important when growing thick oxides as the rate decreases significantly with increasing oxide thickness. The increased oxidation rate in the wet oxidation compared to dry oxidation comes from the higher diffusivity of H_2O through the oxide layer in comparison with O_2. The difference in rate becomes clear when oxidizing a 1 μm layer of SiO_2 as dry oxidation takes 48 hours while wet oxidation takes 2 hours. In optical waveguide systems, typical oxide thicknesses of around 1-4 μm are used in order to avoid leakage of light from the waveguide to the substrate.

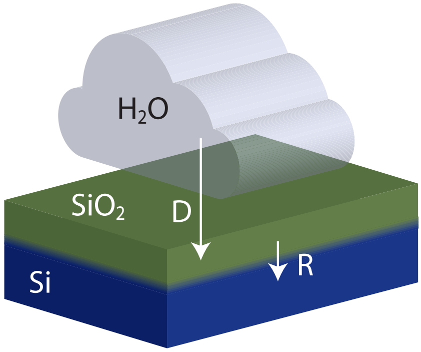

Figure 5.2: Schematic of the wet oxidation process of silicon where water vapor H_2O is used as the oxidant. The diffusion of oxygen atoms is labeled by D and the chemical oxidation reaction is labeled by R.

In the fabrication processes of Paper B and Paper A thermal wet oxidation was used. An oxide around 3 μm was grown in Paper B where high confinement waveguides were fabricated. For the unconventional low confinement waveguide presented in Paper A an oxide thickness of 15 μm was grown in order to avoid substrate leakage [22].

5.4 Thin film deposition

In order to deposit thin films of dedicated materials, several deposition techniques are available in the CMOS library of micro- and nanofabrication. The principle of all techniques is based on the transition of materials from a molecular movable state (gaseous or liquid) to the solid state to form a deposit on top of a wafer substrate. To prepare molecules for precipitation on a substrate, physical or chemical reactions can be utilized. Common physical deposition processes are evaporation and sputtering where vaporized material condensates on a substrate. Vaporization of the deposition material is done by thermal heating of the source (evaporation) or by energetic ion bombardment (sputtering). A thin film deposition technique based on chemical reactions is called CVD. In the CVD process gaseous chemicals react at the wafer surface to start a chemical deposition process. The activation energy for the chemical reaction to happen is commonly thermal or plasma assisted, naming the CVD process either low-pressure chemical vapor deposition (LPCVD) or plasma-enhanced chemical vapor deposition (PECVD).

5.4.1 LPCVD

In LPCVD processes the chemical reaction is driven by temperature. Typical temperature values in the LPCVD reaction chamber are around 700-800 °C. The atomic composition of the precursor gases pumped into the reaction chamber defines the material composition of the deposited film. Changing the gas flow of the individual precursor gases can change the atomic composition of the deposit. This also enables *in-situ* doping of films by adding other gaseous chemicals. The precursor gases are introduced into the reaction chamber in non-reactive form and start to decompose once reaching the hot substrate region in the reactor where the decomposed reaction products deposit. The benefit of having a low pressure in the chamber of around 0.1 to 1.0 torr is that gas phase nucleation is minimized resulting in formation of solid clusters of atoms only on the wafer surface. This leads to high uniformity of the deposited film. Two different types of reactors are used, cold wall and hot wall reactors. In cold wall reactors the deposition reaction only takes place at the surface of the wafer. Hot wall reactors on the other hand have a more uniform distribution of temperature and reduced convection effects, but a film is deposited at the reactor wall leading to a memory effect of the chamber. Common materials deposited with LPCVD are silicon nitrides and silicon dioxide. In the manufacturing process of Paper B and Paper A the deposition of silicon nitride was done using LPCVD. It is important to distinguish between the deposition of stoichiometric silicon nitride in Paper A and of non-stoichiometric silicon nitride in Paper B.

5.4.2 PECVD

The primary nonthermal energy source which is used to drive a CVD-based process is the radio frequency (RF) plasma. Therefore the PECVD process offers the advantage of distinct reduction of process temperatures in comparison to LPCVD. Typical deposition temperatures for PECVD processes are around 200-400 °C. These fairly low temperatures feature an increased substrate protection and allow film deposition on top of temperature-critical substrates (e.g. metalization layers). Common materials for deposition in a PECVD system are silicon-based oxides and nitrides that are mainly used for passivation. Furthermore, the RF power of the plasma is an additional parameter that offers control over the deposited film properties.

5.4.3 Silicon nitride deposition by LPCVD and PECVD

The deposition of silicon nitride as a material for waveguide cores has been shown in both LPCVD [112] and PECVD [23] processes. The film quality of LPCVD nitride is in general higher compared to an LPCVD nitride. This comes from the 15-30% higher hydrogen content in PECVD nitrides resulting in larger optical absorption at telecom wavelength [113]. Furthermore, PECVD nitrides have a higher pinhole density [113]. The stress in thick films of deposited stoichiometric silicon nitride (indicated in section 4.3.2) used for optical waveguides and micro-electro-mechanical systems (MEMS) devices [114] can give rise to cracks in the layers. One approach to avoid film cracks is to change the content of silicon and nitrogen from stoichiometric (Si_3N_4) to silicon enriched. This has been shown with LPCVD in Paper B and [99] and also with PECVD in [98]. Another alternative to reduce the film stress in silicon nitride film is by depositing different layers at alternating RF frequencies of the plasma [91, 115, 116].

5.5 Reactive ion etching

To transfer the pattern from an etch mask into the substrate, an etching procedure is required. In general etching can be carried out in the form of wet or dry etching. Wet etching is mostly isotropic[1] and performed in an etch bath where the pure chemical process can offer a high etch selectivity between materials. Dry etching on the other hand provides an anisotropic etch. This enables better control over the process in comparison to wet etching because there are more available process parameters in dry etching. One special form of dry etching is ion milling where ionized molecules are accelerated in an electric field towards the target substrate. The bombardment of ions with high kinetic energy towards the wafer surface leads to the constant sputtering of surface molecules. This pure physical process appeals to a high degree of anisotropy, but typically has low selectivity [62].
A dry etching process that can provides both selectivity and anisotropy simultaneously is reactive-ion etching (RIE) by supporting both chemical and physical etching properties. RIE is commonly used to etch silicon based materials (e.g. Si, SiO_2, Si_xN_y) with halogen-based etch chemicals (e.g. CHF_3, CF_4). The physical component of the etching comes from electrical-field-assisted acceleration of ionized species toward the surface of the wafer similar to the ion milling process. The chemical component comes from the gaseous etching chemicals used in the process that are ionized and broken down by the plasma inside the etch chamber to form chemically reactive species. The radical species undergo a chemical reaction and break the bonds of surface atoms on the wafer. In this process the binding of surface atoms to reactive radicals becomes energetically favored so that volatile reaction products are formed that are exhausted from the etching chamber. The chosen carbon containing

[1] An isotropic etching process is characterized by the same etching speed in all directions. Exception for this etch behavior is the wet etching in materials like silicon where the etching can be directed by the crystal planes allowing to wet etch in anisotropic manner.

etch chemicals leave reaction by-products like carbon that form polymer coatings on the wafer. This carbon deposit is removed by physical collisions with incident ions. As the impact of ions are lower on vertical sidewall, the polymer sidewall passivation assists anisotropic etching. In Paper B and Paper A the etching of the silicon nitride layers was performed in an RIE process.

Chapter 6

Future outlook

Comb generation
The potential of the thick high-confinement Si_xN_y waveguides for more advanced device structures has been shown in Paper B with the presentation of a fabricated microring resonator. The ring resonator is an important device to achieve Kerr frequency combs [90]. With the rings fabricated, one future project is to achieve comb generation. Important for the comb performance is a minimum optical power P in the ring approximated by [117] $P = \frac{2\alpha^2}{\gamma L}$, where α is the optical roundtrip loss (including ring coupling loss) in the ring, γ is the nonlinear parameter and L is the ring circumference. With our design (γ = 6/W/m, loss = 1.5 dB/cm) the power threshold in a 60 μm ring would be around 80 mW. This is still inefficient since the power indicates the threshold for which parametric oscillation will occur. One needs to increase the pump power further to generate more lines and have broadband combs. However, the equation shows an inverse quadratic dependence with the parameter α. This means that if the losses are reduced by a factor of 2 it results in a 6 dB reduction of the needed power, thus highlighting the importance of decreasing the losses.

Improved propagation loss
A reduced power threshold for parametric oscillation can be achieved with lower waveguide propagation loss. Although the silicon rich nitride Si_xN_y presented in Paper B has higher nonlinearities compared to Si_3N_4, the propagation loss is still high. In high-confinement Si_3N_4 waveguides losses of 0.4 dB/cm has been achieved [21]. Even 0.001 dB/cm has been achieved in low-confinement Si_3N_4 waveguides [22]. One future project is to optimize the material composition of Si_xN_y by changing the content of silicon and nitrogen in order to

reduce the optical propagation loss, while keeping high nonlinearities.

Improved coupling

Further improvement of the integrated waveguide system can be achieved by increasing the coupling efficiency from fiber to waveguide. This would give more optical power coupled into the waveguide and a directly improved nonlinear interaction in the system. To improve the current 4-5 dB coupling loss per facet, a better mode matching of tapered fiber (spot size of 2-3 μm) and integrated waveguide (effective area around 1 μm^2) is required by implementing a spot size converter. To fabricate a spot size converter, like the adiabatic inverse taper [44], a tapering of the waveguide below 150 nm is needed. To resolve features with these dimensions, different lithography tools for improved resolution are required. Electron beam lithography and possibly laser writing are options in the future.

Another option for coupling improvement is an increase in mechanical stability in the end-fire coupling by implementing V-grooves. The use of V-grooves has been presented in [95] in order to provide self-alignment regions for the fiber. V-grooves are essentially trenches in front of the waveguide to support the fiber placement and alignment. A dry and wet etching procedure suitable to etch the V-groove into the silica cladding and silicon substrate under the waveguide core will be developed in the future.

Dispersion engineering of thin low-loss waveguides

The thin low-confinement waveguides presented in Paper A show very good propagation loss of only 0.06 dB/cm. The drawback is that it is not possible to achieve anomalous GVD with such thin structures in a rectangular geometry, as required for highly efficient nonlinear FWM. A recent numerical proposal however shows that by stacking laterally or on top of each other thin silicon nitride waveguides it is possible to engineer the dispersion anywhere within the whole transparency window of silicon nitride. The approach is based on inducing modal coupling between the individual systems. Hence, the supermode may display anomalous dispersion [118]. The lower confinement in the waveguides comes along with a higher bending loss which means that the achievement of narrow spaced frequency combs is challenging in this platform. An increase of footprint in these systems is expected owing the increased bending loss. Nevertheless, the low-loss performance with the option to fulfill the phase-matching condition could prove feasible to achieve the long sought goal of on-chip net-gain based on CW-pumped parametric amplification.

Chapter 7

Summary of papers

Paper A

“Continuous wave-pumped wavelength conversion in low-loss silicon nitride waveguides,” Continuous wave-pumped wavelength conversion in low-loss silicon nitride waveguides *Optics Letters*, vol. 40, no. 6, pp. 875-878, 2015.

This paper presents the linear and nonlinear characterization of low-loss low-confinement waveguides fabricated from stoichiometric silicon nitride. These waveguides were fabricated by the group of John Bowers (University of California Santa Barbara). The 100 nm thin waveguide core leads to low optical confinement and results in low propagation loss of 0.06 dB/cm. In a nonlinear FWM experiment the nonlinear parameter has been estimated and in a wavelength conversion experiment all-optical processing of 10 Gb/s OOK data has been demonstrated. This paper shows that a similar conversion efficiency to SOI waveguides could be achieved with Si_3N_4, despite the inherently lower nonlinear coefficient.

Paper B

“Linear and nonlinear characterization of low-stress high-confinement silicon-rich nitride waveguides,” *Optics Express*, vol. 23, no. 20, pp. 25828-25837, 2015.

This paper presents the fabrication, simulation and characterization of high-confinement waveguides based on non-stoichiometric silicon nitride. This waveguide platform was developed at Chalmers. In loss measurements the propagation and coupling loss has been shown in a wavelength-resolved manner and the contribution of the scattering loss has been evaluated. In mode-solver simulations the dispersion and confinement properties in terms of the waveguides dimensions has been studied. Nonlinear FWM experiments has been shown and the functionality of a microring resonator has been presented, displaying high-quality factors $\sim 10^5$ in the 1.5 μm wavelength regime.

Bibliography

[1] K. C. Kao and G. A. Hockham, "Dielectric-fibre surface waveguide for optical frequencies," *Procedings of the IEE*, vol. 113, no. 7, pp. 1151–1158, 1966.

[2] D. A. B. Miller, "Optical interconnects to silicon," *IEEE Journal on Selected Topics in Quantum Electronics*, vol. 6, no. 6, pp. 1312–1317, 2000.

[3] J. W. Goodman, F. J. Leonberger, S.-Y. Kung, and R. A. Athale, "Optical interconnections for VLSI systems," *Proceedings of the IEEE*, vol. 72, no. 7, pp. 850–866, 1984.

[4] T. H. Maiman, "Stimulated optical radiation in ruby," *Nature*, vol. 187, no. 4736, pp. 493–494, 1960.

[5] J. A. Tatum, D. Gazula, L. A. Graham, J. K. Guenter, R. H. Johnson, J. King, C. Kocot, G. D. Landry, I. Lyubomirsky, A. N. MacInnes, E. M. Shaw, K. Balemarthy, R. Shubochkin, D. Vaidya, M. Yan, and F. Tang, "VCSEL-based interconnects for current and future data centers," *Journal of Lightwave Technology*, vol. 33, no. 4, pp. 727–732, 2015.

[6] A. Larsson, "Advances in VCSELs for communication and sensing," *IEEE Journal of Selected Topics in Quantum Electronics*, vol. 17, no. 6, pp. 1552–1567, 2011.

[7] M. Chacinski, N. Chitica, S. Molin, N. Lalic, and O. Sahlén, "25.78Gbps data transmission with 850nm multimode VCSEL packaged in QSFP form factor module," *Optical Fiber Communication Conference and Exposition and the National Fiber Optic Engineers Conference OW1B.1*, 2013.

[8] A. Huang, C. Gunn, G.-L. Li, Y. Liang, S. Mirsaidi, A. Narasimha, and T. Pinguet, "MUX / DEMUX integrated with electronics," *Solid-State Circuit Conference*, 2006.

[9] D. Mahgerefteh, C. Thompson, C. Cole, G. Denoyer, T. Nguyen, I. Lyubomirsky, C. Kocot, and J. Tatum, "Techno-economic comparison of silicon photonics and multimode VCSELs," *Optical Fiber Communication Conference M3B.2*, 2015.

[10] R. A. Soref and J. P. Lorenzo, "All-silicon active and passive guided-wave components for $\lambda = 1.3$ and 1.6 μm," *IEEE Journal on Selected Topics in Quantum Electronics*, vol. QE-22, no. 6, pp. 873–879, 1986.

[11] U. Fischer, T. Zinke, J.-R. Kropp, F. Arndt, and K. Petermann, "0.1 dB/cm waveguide losses in single-mode SOI rib waveguides," *IEEE Photonics Technology Letters*, vol. 8, no. 5, pp. 647–648, 1996.

[12] M. J. R. Heck, H.-W. Chen, A. W. Fang, B. R. Koch, D. Liang, H. Park, M. N. Sysak, and J. E. Bowers, "Hybrid silicon photonics for optical interconnects," *IEEE Journal of Selected Topics in Quantum Electronics*, vol. 17, no. 2, pp. 333–346, 2011.

[13] M. Hochberg and T. Baehr-Jones, "Towards fabless silicon photonics," *Nature Photonics*, vol. 4, no. 8, pp. 492–494, 2010.

[14] J. Leuthold, C. Koos, and W. Freude, "Nonlinear silicon photonics," *Nature Photonics*, vol. 4, no. 8, pp. 535–544, 2010.

[15] R. Salem, M. A. Foster, A. C. Turner, D. F. Geraghty, M. Lipson, and A. L. Gaeta, "Signal regeneration using low-power four-wave mixing on silicon chip," *Nature Photonics*, vol. 2, no. 1, pp. 35–38, 2007.

[16] M. A. Foster, A. C. Turner, R. Salem, M. Lipson, and A. L. Gaeta, "Broad-band continuous-wave parametric wavelength conversion in silicon nanowaveguides," *Optics Express*, vol. 15, no. 20, pp. 12949–12958, 2007.

[17] I.-W. Hsieh, X. Chen, X. Liu, J. I. Dadap, N. C. Panoiu, C.-Y. Chou, F. Xia, W. M. Green, Y. A. Vlasov, and R. M. Osgood, Jr., "Supercontinuum generation in silicon photonic wires," *Optics Express*, vol. 15, no. 23, pp. 15242–15249, 2007.

[18] A. D. Bristow, N. Rotenberg, and H. M. van Driel, "Two-photon absorption and Kerr coefficients of silicon for 850-2200 nm," *Applied Physics Letters*, vol. 90, no. 19, pp. 191104–3, 2007.

[19] M. Dinu, F. Quochi, and H. Garcia, "Third-order nonlinearities in silicon at telecom wavelengths," *Applied Physics Letters*, vol. 82, no. 18, pp. 2954–2956, 2003.

[20] J. Bauer, "Optical properties, band gap, and surface roughness of Si_3N_4," *Physica Status Solidi (a)*, vol. 39, no. 2, pp. 411–418, 1977.

[21] D. J. Moss, R. Morandotti, A. L. Gaeta, and M. Lipson, "New CMOS-compatible platforms based on silicon nitride and Hydex for nonlinear optics," *Nature Photonics*, vol. 7, no. 8, pp. 597–607, 2013.

[22] J. F. Bauters, M. J. R. Heck, D. D. John, J. S. Barton, C. M. Bruinink, A. Leinse, R. G. Heideman, D. J. Blumenthal, and J. E. Bowers, "Planar waveguides with less than 0.1 dB/m propagation loss fabricated with wafer bonding," *Optics Express*, vol. 19, no. 24, pp. 24090–24101, 2011.

[23] K. Ikeda, R. E. Saperstein, N. Alic, and Y. Fainman, "Thermal and Kerr nonlinear properties of plasma-deposited silicon nitride/ silicon dioxide waveguides," *Optics Express*, vol. 16, no. 17, pp. 12987–12994, 2008.

[24] Y. Okawachi, K. Saha, J. S. Levy, Y. H. Wen, M. Lipson, and A. L. Gaeta, "Octave-spanning frequency comb generation in a silicon nitride chip," *Optics Letters*, vol. 36, no. 17, pp. 3398–3400, 2011.

[25] J. P. Epping, T. Hellwig, M. Hoekman, R. Mateman, A. Leinse, R. G. Heideman, A. van Rees, P. J. van der Slot, C. J. Lee, C. Fallnich, and K.-J. Boller, "On-chip visible-to-infrared supercontinuum generation with more than 495 THz spectral bandwidth," *Optics Express*, vol. 23, no. 15, pp. 19596–19604, 2015.

[26] K. Luke, A. Dutt, C. B. Poitras, and M. Lipson, "Overcoming Si_3N_4 film stress limitations for high quality factor ring resonators," *Optics Express*, vol. 21, no. 19, pp. 22829–22833, 2013.

[27] S. Habermehl, "Stress relaxation in Si-rich silicon nitride thin films," *Journal of Applied Physics*, vol. 83, no. 9, pp. 4672–4677, 1998.

[28] G. P. Agrawal, *Nonlinear Fiber Optics.* Academic Press, 5th ed., 2013.

[29] M. C. Petty, *Molecular Electronics.* Intersience, 2007.

[30] F. Träger, ed., *Handbook of Lasers and Optics.* Springer, 2nd ed., 2012.

[31] R. W. Boyd, *Nonlinear Optics.* Academic Press, 1992.

[32] B. E. A. Saleh and M. C. Teich, *Fundamentals of Photonics.* Interscience, 2nd ed., 2007.

[33] C. Koos, L. Jacome, C. Poulton, J. Leuthold, and W. Freude, "Nonlinear silicon-on-insulator waveguides for all-optical signal processing," *Optics Express*, vol. 15, no. 10, pp. 5976–5990, 2007.

[34] C.-L. Chen, *Foundations for guided-wave optics.* John Wiley & Sons, Inc., 2007.

[35] W. D. Sacher, Y. Huang, G.-Q. Lo, and J. K. S. Poon, "Multilayer silicon nitride-on-silicon integrated photonic platforms and devices," *Journal of Lightwave Technology*, vol. 33, no. 4, pp. 901–910, 2015.

[36] M. R. Watts, H. A. Haus, and E. P. Ippen, "Integrated mode-evolution-based polarization splitter," *Optics Letters*, vol. 30, no. 9, pp. 967–969, 2005.

[37] J. F. Bauters, M. J. R. Heck, D. Dai, J. S. Barton, D. J. Blumenthal, and J. E. Bowers, "Ultralow-loss planar Si_3N_4 waveguide polarizers," *IEEE Photonics Journal*, vol. 5, no. 1, p. 6600207, 2013.

[38] C. Li, J. H. Song, J. Zhang, H. Zhang, S. Chen, M. Yu, and G. Q. Lo, "Silicon polarization independent microring resonator-based optical tunable filter circuit with fiber assembly," *Optics Express*, vol. 19, no. 16, pp. 15429–15437, 2011.

[39] R. G. Hunsperger, *Integrated Optics.* Springer-Verlag, 4th ed., 1995.

[40] J. Lacey and F. Payne, "Radiation loss from planar waveguides with random wall imperfections," *IEE Proceedings*, vol. 137, no. 4, pp. 282–288, 1990.

[41] S. K. Selvaraja, P. Jaenen, W. Bogaerts, D. Van Thourhout, P. Dumon, and R. Baets, "Fabrication of photonic wire and crystal circuits in silicon-on-insulator using 193-nm optical lithography," *Journal of Lightwave Technology*, vol. 27, no. 18, pp. 4076–4083, 2009.

[42] B. J. Eggleton, B. Luther-Davies, and K. Richardson, "Chalcogenide photonics," *Nature Photonics*, vol. 5, no. 3, pp. 141–148, 2011.

[43] A. Gajda, L. Zimmermann, M. Jazayerifar, G. Winzer, H. Tian, R. Elschner, T. Richter, C. Schubert, B. Tillack, and K. Petermann, "Highly efficient CW parametric conversion at 1550 nm in SOI waveguides by reverse biased p-i-n junction," *Optics Express*, vol. 20, no. 12, pp. 13100–13107, 2012.

[44] M. Itoh, T. Saida, Y. Hida, M. Ishii, Y. Inoue, Y. Hibino, and A. Sugita, "Large reduction of singlemode-fibre coupling loss in 1.5% planar lightwave circuits using spot-size converters," *Electronics Letters*, vol. 38, no. 2, pp. 72–74, 2002.

[45] D. Taillaert, P. Bienstman, and R. Baets, "Compact efficient broadband grating coupler for silicon-on-insulator waveguides," *Optics Letters*, vol. 29, no. 23, pp. 2749–2751, 2004.

[46] W. S. Zaoui, A. Kunze, W. Vogel, M. Berroth, J. Butschke, F. Letzkus, and J. Burghartz, "Bridging the gap between optical fibers and silicon photonic integrated circuits," *Optics Express*, vol. 22, no. 2, pp. 1277–1286, 2014.

[47] X. Gai, S. Madden, D.-Y. Choi, D. Bulla, and B. Luther-Davies, "Dispersion engineered $Ge_{11.5}As_{24}Se_{64.5}$ nanowires with a nonlinear parameter of $136W^{-1}m^{-1}$ at 1550nm," *Optics Express*, vol. 18, no. 18, pp. 18866–18874, 2010.

[48] A. Prasad, C.-j. Zha, R.-p. Wang, A. Smith, S. Madden, and B. Luther-Davies, "Properties of $Ge_xAs_ySe_{1-x-y}$ glasses for all-optical signal processing," *Optics Express*, vol. 16, no. 4, pp. 2804–2815, 2008.

[49] M. R. Lamont, B. Luther-Davies, D.-Y. Choi, S. Madden, and B. J. Eggleton, "Supercontinuum generation in dispersion engineered highly nonlinear ($\gamma = 10$ /W/m) As_2S_3 chalcogenide planar waveguide," *Optics Express*, vol. 16, no. 19, pp. 14938–14944, 2008.

[50] R. Neo, J. Schröder, Y. Paquot, D.-y. Choi, S. Madden, B. Luther-Davies, and B. J. Eggleton, "Phase-sensitive amplification of light in a $\chi(3)$ photonic chip using a dispersion engineered chalcogenide ridge waveguide," *Optics Express*, vol. 21, no. 7, pp. 7926–7933, 2013.

[51] M. R. E. Lamont, B. Luther-Davies, D.-Y. Choi, S. Madden, X. Gai, and B. J. Eggleton, "Net-gain from a parametric amplifier on a chalcogenide optical chip," *Optics Express*, vol. 16, no. 25, pp. 20374–20381, 2008.

[52] M. R. E. Lamont, V. G. Ta'eed, M. A. F. Roelens, D. J. Moss, B. J. Eggleton, D.-Y. Choi, S. Madden, and B. Luther-Davies, "Error-free wavelength conversion via cross-phase modulation in 5 cm of As_2S_3 chalcogenide glass rib waveguide," *Electronics Letters*, vol. 43, no. 17, pp. 16–17, 2007.

[53] F. Luan, M. D. Pelusi, M. R. E. Lamont, D.-Y. Choi, S. Madden, B. Luther-Davies, and B. J. Eggleton, "Dispersion engineered As_2S_3 planar waveguides for broadband four-wave mixing based wavelength conversion of 40 Gb/s signals," *Optics Express*, vol. 17, no. 5, pp. 3514–3520, 2009.

[54] V. G. Ta'eed, M. Shokooh-Saremi, L. Fu, D. J. Moss, M. Rochette, I. C. M. Littler, B. J. Eggleton, Y. Ruan, and B. Luther-Davies, "Integrated all-optical pulse regenerator in chalcogenide waveguides," *Optics Letters*, vol. 30, no. 21, pp. 2900–2902, 2005.

[55] W. Astar, P. Apiratikul, T. E. Murphy, and G. M. Carter, "Wavelength conversion of 10-Gb/s RZ-OOK using filtered XPM in a passive GaAs-AlGaAs waveguide," *IEEE Photonics Technology Letters*, vol. 22, no. 9, pp. 637–639, 2010.

[56] M. Pu, L. Ottaviano, E. Semenova, and K. Yvind, "AlGaAs-On-Insulator nonlinear photonics," *arXiv:1509.03620*, 2015.

[57] P. Apiratikul, J. J. Wathen, G. A. Porkolab, B. Wang, L. He, T. E. Murphy, and C. J. K. Richardson, "Enhanced continuous-wave four-wave mixing efficiency in nonlinear AlGaAs waveguides," *Optics Express*, vol. 22, no. 22, pp. 26814–26824, 2014.

[58] C. Lacava, V. Pusino, P. Minzioni, M. Sorel, and I. Cristiani, "Nonlinear properties of AlGaAs waveguides in continuous wave operation regime," *Optics Express*, vol. 22, no. 5, pp. 5291–5298, 2014.

[59] P. P. Absil, J. V. Hryniewicz, B. E. Little, P. S. Cho, R. A. Wilson, L. G. Joneckis, and P.-T. Ho, "Wavelength conversion in GaAs micro-ring resonators," *Optics Letters*, vol. 25, no. 8, pp. 554–556, 2000.

[60] M. Pu, H. Hu, L. Ottaviano, E. Semenova, D. Vukovic, L. Oxenløwe, and K. Yvind, "AlGaAs-on-insulator nanowire with 750 nm FWM bandwidth, -9 dB CW conversion efficiency, and ultrafast operation enabling record Tbaud wavelength conversion," *Optical Fiber Communication Conference Th5A.3*, 2015.

[61] M. Pu, L. Ottaviano, E. Semenova, L. K. Oxenløwe, and K. Yvind, "Ultra-Low Threshold Power On-Chip Optical Parametric Oscillation in AlGaAs-On-Insulator Microresonator," *Proceedings of the Conference on Lasers and Electro-Optics JTh5A.9*, 2015.

[62] S. A. Campbell, *The Science and Engineering of Microelectronic Fabrication.* Oxford University Press, 3rd ed., 2008.

[63] G. K. Celler and S. Cristoloveanu, "Frontiers of silicon-on-insulator," *Journal of Applied Physics*, vol. 93, no. 9, pp. 4955–4978, 2003.

[64] E. Dulkeith, Y. a. Vlasov, X. Chen, N. C. Panoiu, and R. M. Osgood, Jr., "Self-phase-modulation in submicron silicon-on-insulator photonic wires," *Optics Express*, vol. 14, no. 12, pp. 5524–5534, 2006.

[65] A. C. Turner-Foster, M. A. Foster, J. S. Levy, C. B. Poitras, R. Salem, A. L. Gaeta, and M. Lipson, “Ultrashort free-carrier lifetime in low-loss silicon nanowaveguides,” *Optics Express*, vol. 18, no. 4, pp. 3582–3591, 2010.

[66] F. Da Ros, D. Vukovic, A. Gajda, K. Dalgaard, L. Zimmermann, B. Tillack, M. Galili, K. Petermann, and C. Peucheret, “Phase regeneration of DPSK signals in a silicon waveguide with reverse-biased p-i-n junction.,” *Optics Express*, vol. 22, no. 5, pp. 5029–5036, 2014.

[67] B. Corcoran, C. Monat, C. Grillet, D. J. Moss, B. J. Eggleton, T. P. White, L. O’Faolain, and T. F. Krauss, “Green light emission in silicon through slow-light enhanced third-harmonic generation in photonic-crystal waveguides,” *Nature Photonics*, vol. 3, no. 4, pp. 206–210, 2009.

[68] B. Kuyken, X. Liu, G. Roelkens, R. Baets, R. M. Osgood, Jr., and W. M. J. Green, “50 dB parametric on-chip gain in silicon photonic wires,” *Optics Letters*, vol. 36, no. 22, pp. 4401–4403, 2011.

[69] M. a. Foster, A. C. Turner, J. E. Sharping, B. S. Schmidt, M. Lipson, and A. L. Gaeta, “Broad-band optical parametric gain on a silicon photonic chip,” *Nature*, vol. 441, pp. 960–963, 2006.

[70] R. L. Espinola, J. I. Dadap, R. M. Osgood, Jr, S. J. McNab, and Y. A. Vlasov, “C-band wavelength conversion in silicon photonic wire waveguides,” *Optics Express*, vol. 13, no. 11, pp. 4341–4349, 2005.

[71] A. C. Turner, M. A. Foster, A. L. Gaeta, and M. Lipson, “Ultra-low power parametric frequency conversion in a silicon microring resonator,” *Optics Express*, vol. 16, no. 7, pp. 4881–4887, 2008.

[72] H. Fukuda, K. Yamada, T. Shoji, M. Takahashi, T. Tsuchizawa, T. Watanabe, J.-I. Takahashi, and S.-I. Itabashi, “Four-wave mixing in silicon wire waveguides,” *Optics Express*, vol. 13, no. 12, pp. 4629–4637, 2005.

[73] W. Mathlouthi, H. Rong, and M. Paniccia, “Characterization of efficient wavelength conversion by four-wave mixing in sub-micron silicon waveguides,” *Optics Express*, vol. 16, no. 21, pp. 16735–16745, 2008.

[74] Y.-H. Kuo, H. Rong, V. Sih, S. Xu, M. Paniccia, and O. Cohen, “Demonstration of wavelength conversion at 40 Gb/s data rate in silicon waveguides,” *Optics Express*, vol. 14, no. 24, pp. 11721–11726, 2006.

[75] K. Ikeda, Y. Shen, and Y. Fainman, “Enhanced optical nonlinearity in amorphous silicon and its application to waveguide devices,” *Optics Express*, vol. 15, no. 26, pp. 17761–17771, 2007.

[76] A. Harke, M. Krause, and J. Mueller, "Low-loss singlemode amorphous silicon waveguides," *Electronic Letters*, vol. 41, no. 25, pp. 41–42, 2005.

[77] B. Kuyken, H. Ji, S. Clemmen, S. K. Selvaraja, H. Hu, M. Pu, M. Galili, P. Jeppesen, G. Morthier, S. Massar, L. K. Oxenløwe, G. Roelkens, and R. Baets, "Nonlinear properties of and nonlinear processing in hydrogenated amorphous silicon waveguides," *Optics Express*, vol. 19, no. 26, pp. B146–B153, 2011.

[78] Y. Shoji, T. Ogasawara, T. Kamei, Y. Sakakibara, S. Suda, K. Kintaka, H. Kawashima, M. Okano, T. Hasama, H. Ishikawa, and M. Mori, "Ultrafast nonlinear effects in hydrogenated amorphous silicon wire waveguide.," *Optics Express*, vol. 18, no. 6, pp. 5668–5673, 2010.

[79] S. Suda, K. Tanizawa, Y. Sakakibara, T. Kamei, K. Nakanishi, E. Itoga, T. Ogasawara, R. Takei, H. Kawashima, S. Namiki, M. Mori, T. Hasama, and H. Ishikawa, "Pattern-effect-free all-optical wavelength conversion using a hydrogenated amorphous silicon waveguide with ultra-fast carrier decay," *Optics Letters*, vol. 37, no. 8, pp. 1382–1384, 2012.

[80] B. Kuyken, S. Clemmen, S. K. Selvaraja, W. Bogaerts, D. V. Thourhout, P. Emplit, S. Massar, G. Roelkens, and R. Baets, "On-chip parametric amplification with 26.5 dB gain at telecommunication wavelengths using CMOS-compatible hydrogenated amorphous silicon waveguides," *Optics Letters*, vol. 36, no. 4, pp. 552–554, 2011.

[81] C. Grillet, L. Carletti, C. Monat, P. Grosse, B. Ben Bakir, S. Menezo, J. M. Fedeli, and D. J. Moss, "Amorphous silicon nanowires combining high nonlinearity, FOM and optical stability," *Optics Express*, vol. 20, no. 20, pp. 22609–22615, 2012.

[82] K. Narayanan and S. F. Preble, "Optical nonlinearities in hydrogenated-amorphous silicon waveguides," *Optics Express*, vol. 18, no. 9, pp. 8998–9005, 2010.

[83] K.-Y. Wang and A. C. Foster, "Ultralow power continuous-wave frequency conversion in hydrogenated amorphous silicon waveguides," *Optics Letters*, vol. 37, no. 8, pp. 1331–1333, 2012.

[84] J. Matres, G. C. Ballesteros, P. Gautier, J.-M. Fédéli, J. Martí, and C. J. Oton, "High nonlinear figure-of-merit amorphous silicon waveguides," *Optics Express*, vol. 21, no. 4, pp. 3932–3940, 2013.

[85] J. Safioui, F. Leo, B. Kuyken, S.-P. Gorza, S. K. Selvaraja, R. Baets, P. Emplit, G. Roelkens, and S. Massar, "Supercontinuum generation in

hydrogenated amorphous silicon waveguides at telecommunication wavelengths," *Optics Express*, vol. 22, no. 3, pp. 3089–3097, 2014.

[86] U. D. Dave, S. Uvin, B. Kuyken, S. Selvaraja, F. Leo, and G. Roelkens, "Telecom to mid-infrared spanning supercontinuum generation in hydrogenated amorphous silicon waveguides using a Thulium doped fiber laser pump source," *Optics Express*, vol. 21, no. 26, pp. 32032–32039, 2013.

[87] D. T. Spencer, J. F. Bauters, M. J. R. Heck, and J. E. Bowers, "Integrated waveguide coupled Si_3N_4 in the ultrahigh-Q regime," *Optica*, vol. 1, no. 3, pp. 153–157, 2014.

[88] D. T. H. Tan, K. Ikeda, P. C. Sun, and Y. Fainman, "Group velocity dispersion and self phase modulation in silicon nitride waveguides," *Applied Physics Letters*, vol. 96, pp. 061101–3, 2010.

[89] A. Gondarenko, J. S. Levy, and M. Lipson, "High confinement micron-scale silicon nitride high Q ring resonator.," *Optics Express*, vol. 17, no. 14, pp. 11366–11370, 2009.

[90] J. S. Levy, A. Gondarenko, M. A. Foster, A. C. Turner-Foster, A. L. Gaeta, and M. Lipson, "CMOS-compatible multiple-wavelength oscillator for on-chip optical interconnects," *Nature Photonics*, vol. 4, no. 1, pp. 37–40, 2010.

[91] E. van de Ven, I.-W. Connick, and A. S. Harrus, "Advantages of dual frequency PECVD for deposition of ILD and passivation films," *LSI Multilevel Interconnection, International IEEE Conference TH-0325*, pp. 194–201, 1990.

[92] J. P. Epping, M. Hoekman, R. Mateman, A. Leinse, R. G. Heideman, A. van Rees, P. J. van der Slot, C. J. Lee, and K.-J. Boller, "High confinement, high yield Si_3N_4 waveguides for nonlinear optical applications," *Optics Express*, vol. 23, no. 2, pp. 642–648, 2015.

[93] R. Halir, Y. Okawachi, J. S. Levy, M. A. Foster, M. Lipson, and A. L. Gaeta, "Ultrabroadband supercontinuum generation in a CMOS-compatible platform," *Optics Letters*, vol. 37, no. 10, pp. 1685–1687, 2012.

[94] J. S. Levy, M. A. Foster, A. L. Gaeta, and M. Lipson, "Harmonic generation in silicon nitride ring resonators," *Optics Express*, vol. 19, no. 12, pp. 11415–11421, 2011.

[95] F. Ferdous, H. Miao, D. E. Leaird, K. Srinivasan, J. Wang, L. Chen, L. T. Varghese, and A. M. Weiner, "Spectral line-by-line pulse shaping

of an on-chip microresonator frequency comb," *Nature Photonics*, vol. 5, no. 12, pp. 770–776, 2011.

[96] A. R. Johnson, Y. Okawachi, J. S. Levy, J. Cardenas, K. Saha, M. Lipson, and A. L. Gaeta, "Chip-based frequency combs with sub-100 GHz repetition rates," *Optics Letters*, vol. 37, no. 5, pp. 875–877, 2012.

[97] T. Herr, K. Hartinger, J. Riemensberger, C. Y. Wang, E. Gavartin, R. Holzwarth, M. L. Gorodetsky, and T. J. Kippenberg, "Universal formation dynamics and noise of Kerr-frequency combs in microresonators," *Nature Photonics*, vol. 6, pp. 480–487, June 2012.

[98] J. M. Chavez Boggio, D. Bodenmüller, T. Fremberg, R. Haynes, M. M. Roth, R. Eisermann, M. Lisker, L. Zimmermann, and M. Böhm, "Dispersion engineered silicon nitride waveguides by geometrical and refractive-index optimization," *Journal of the Optical Society of America B*, vol. 31, no. 11, pp. 2846–2857, 2014.

[99] H. T. Philipp, K. N. Andersen, W. Svendsen, and H. Ou, "Amorphous silicon rich silicon nitride optical waveguides for high density integrated optics," *Electronics Letters*, vol. 40, no. 7, 2004.

[100] D. Duchesne, M. Peccianti, M. R. E. Lamont, M. Ferrera, L. Razzari, F. Légaré, R. Morandotti, S. Chu, B. E. Little, and D. J. Moss, "Supercontinuum generation in a high index doped silica glass spiral waveguide," *Optics Express*, vol. 18, no. 2, pp. 923–930, 2010.

[101] A. Pasquazi, M. Peccianti, Y. Park, B. E. Little, S. T. Chu, R. Morandotti, J. Azaña, and D. J. Moss, "Sub-picosecond phase-sensitive optical pulse characterization on a chip," *Nature Photonics*, vol. 5, no. 10, pp. 618–623, 2011.

[102] A. Pasquazi, Y. Park, J. Azaña, F. Légaré, R. Morandotti, B. E. Little, S. T. Chu, and D. J. Moss, "Efficient wavelength conversion and net parametric gain via four wave mixing in a high index doped silica waveguide," *Optics Express*, vol. 18, no. 8, pp. 7634–7641, 2010.

[103] A. Pasquazi, R. Ahmad, M. Rochette, M. Lamont, B. E. Little, S. T. Chu, R. Morandotti, and D. J. Moss, "All-optical wavelength conversion in an integrated ring resonator," *Optics Express*, vol. 18, no. 4, pp. 3858–3863, 2010.

[104] M. Peccianti, A. Pasquazi, Y. Park, B. Little, S. Chu, D. Moss, and R. Morandotti, "Demonstration of a stable ultrafast laser based on a nonlinear microcavity," *Nature Communications*, vol. 3, pp. 1–6, 2012.

[105] L. Razzari, D. Duchesne, M. Ferrera, R. Morandotti, S. Chu, B. E. Little, and D. J. Moss, "CMOS-compatible integrated optical hyper- parametric oscillator," *Nature Photonics*, vol. 4, no. 1, pp. 41–45, 2010.

[106] C. Lundström, R. Malik, L. Grüner-Nielsen, B. Corcoran, S. L. I. Olsson, M. Karlsson, and P. A. Andrekson, "Fiber optic parametric amplifier with 10-dB net gain without pump dithering," *IEEE Photonics Technology Letters*, vol. 25, no. 3, pp. 234–237, 2013.

[107] S. J. Madden, D.-Y. Choi, D. A. Bulla, A. V. Rode, B. Luther-Davies, V. G. Ta'eed, M. D. Pelusi, and B. J. Eggleton, "Long, low loss etched As(2)S(3) chalcogenide waveguides for all-optical signal regeneration," *Optics Express*, vol. 15, no. 22, pp. 14414–14421, 2007.

[108] L. Tsybeskov, D. J. Lockwood, and M. Ichikawa, "Silicon photonics: CMOS going optical," *Proceedings of the IEEE*, vol. 97, no. 7, pp. 1161–1165, 2009.

[109] W. Bogaerts, R. Baets, P. Dumon, V. Wiaux, S. Beckx, D. Taillaert, B. Luyssaert, J. Van Campenhout, P. Bienstman, and D. Van Thourhout, "Nanophotonic waveguides in silicon-on-insulator fabricated with CMOS technology," *Journal of Lightwave Technology*, vol. 23, no. 1, pp. 401–412, 2005.

[110] M. Paniccia and N. Photonics, "Integrating silicon photonics," *Nature Photonics*, vol. 4, no. 8, pp. 498–499, 2010.

[111] P. Dumon, W. Bogaerts, R. Baets, J.-M. Fedeli, and L. Fulbert, "Towards foundry approach for silicon photonics: silicon photonics platform ePIXfab," *Electronics Letters*, vol. 45, no. 12, pp. 581–582, 2009.

[112] N. Daldosso, M. Melchiorri, F. Riboli, M. Girardini, G. Pucker, M. Crivellari, P. Bellutti, A. Lui, and L. Pavesi, "Comparison among various Si_3N_4 waveguide geometries grown within a CMOS fabrication pilot line," *Journal of Lightwave Technology*, vol. 22, no. 7, pp. 1734–1740, 2004.

[113] X.-J. Liu, J.-J. Zhang, X.-W. Sun, Y.-B. Pan, L.-P. Huang, and C.-Y. Jin, "Growth and properties of silicon nitride films prepared by low pressure chemical vapor deposition using trichlorosilane and ammonia," *Thin Solid Films*, vol. 460, pp. 72–77, 2004.

[114] C.-K. Chung, M.-Q. Tsai, P.-H. Tsai, and C. Lee, "Fabrication and characterization of amorphous Si films by PECVD for MEMS," *Journal of Micromechanics and Microengineering*, vol. 15, pp. 136–142, 2005.

[115] M. Belyansky, M. Chace, O. Gluschenkov, J. Kempisty, N. Klymko, A. Madan, A. Mallikarjunan, S. Molis, Y. Ronsheim, D. Yang, and Y. Li, "Methods of producing plasma enhanced chemical vapor deposition silicon nitride thin films with high compressive and tensile stress," *Journal of Vacuum Science and Technology A*, vol. 26, no. 3, pp. 517–521, 2008.

[116] A. Gorin, A. Jaouad, E. Grondin, V. Aimez, and P. Charette, "Fabrication of silicon nitride waveguides for visible-light using PECVD: a study of the effect of plasma frequency on optical properties," *Optics Express*, vol. 16, no. 18, pp. 13509–13516, 2008.

[117] V. Torres-Company, D. Castelló-Lurbe, and E. Silvestre, "Comparative analysis of spectral coherence in microresonator frequency combs," *Optics Express*, vol. 22, no. 4, pp. 4678–4691, 2014.

[118] M. Soltani, A. B. Matsko, and L. Maleki, "Enabling Arbitrary Wavelength Optical Frequency Combs on Chip," *arXiv:1509.07902v1*, 2015.

Papers A–B

Paper A

Continuous wave-pumped wavelength conversion in low-loss silicon nitride waveguides

C. J. Krückel, V. Torres-Company, P. A. Andrekson, D. T. Spencer, J. F. Bauters, M. J. R. Heck, and J. E. Bowers,

Optics Letters, vol. 40, no. 6, pp. 875-878, 2015.

Continuous wave-pumped wavelength conversion in low-loss silicon nitride waveguides

Clemens J. Krückel,[1,*] Víctor Torres-Company,[1] Peter A. Andrekson,[1] Daryl T. Spencer,[2] Jared F. Bauters,[2] Martijn J. R. Heck,[2] and John E. Bowers[2]

[1]*Photonics Laboratory, Department of Microtechnology and Nanoscience, Chalmers University of Technology, SE-412 96 Gothenburg, Sweden*

[2]*Department of Electrical and Computer Engineering, University of California, Santa Barbara, California 93106, USA*

**Corresponding author: kruckel@chalmers.se*

Received December 16, 2014; revised January 26, 2015; accepted January 28, 2015; posted January 28, 2015 (Doc. ID 230655); published March 3, 2015

In this Letter we introduce a complementary metal-oxide semiconductor (CMOS)-compatible low-loss Si_3N_4 waveguide platform for nonlinear integrated optics. The waveguide has a moderate nonlinear coefficient of 285 W/km, but the achieved propagation loss of only 0.06 dB/cm and the ability to handle high optical power facilitate an optimal waveguide length for wavelength conversion. We observe a constant quadratic dependence of the four-wave mixing (FWM) process on the continuous-wave (CW) pump when operating in the C-band, which indicates that the waveguide has negligible high-power constraints owing to nonlinear losses. We achieve a conversion efficiency of −26.1 dB and idler power generation of −19.6 dBm. With these characteristics, we present for the first time, to the best of our knowledge, CW-pumped data conversion in a non-resonant Si_3N_4 waveguide.

OCIS codes: (130.3120) Integrated optics devices; (190.4360) Nonlinear optics, devices; (190.4380) Nonlinear optics, four-wave mixing; (190.4390) Nonlinear optics, integrated optics.

http://dx.doi.org/10.1364/OL.40.000875

Photonic integration can lead to drastic reductions in power consumption and the size of optical systems. The integration of photonic systems showing nonlinear phenomena such as four-wave mixing (FWM) enables useful applications for all-optical signal processing such as wavelength conversion [1] or signal regeneration [2] at the chip level. Material platforms suitable for nonlinear integrated optics, including silicon-based compounds (Si, Si_3N_4, SiON, SiO_2) [3–6], chalcogenide glasses [7], and III-V semiconductors (AlGaAs) [8], have been extensively studied for decades. In addition, some of the above materials could be hybridized with extra layers, such as organic composites [9], to further improve the nonlinear performance.

Using the mature technologies of the complementary metal-oxide semiconductor (CMOS) processing platform for integrated optics enables the option for mass production and thus tremendously reduces processing costs. To better understand why silicon nitride is our chosen material, let us turn our attention to the nonlinear phase shift $\Phi_{NL} = \gamma P L_{eff}$. This product of nonlinear coefficient γ, power level P, and effective length L_{eff} must be maximized to achieve high FWM efficiency. As the nonlinear Kerr coefficient of Si_3N_4 is one order of magnitude greater than the one in SiO_2 [10], a higher γ and a more efficient Kerr process is achieved in Si_3N_4. Although Si has even higher nonlinearities, the nonlinear losses originating from two-photon absorption (TPA) and free carrier absorption at telecom wavelengths limit the maximum power levels P that can be sent in this material. The need to operate at moderate power levels means that the energy in the wavelength-converted signal will not be high, regardless of the conversion efficiency (CE). It is of course possible to remove the photogenerated carriers in silicon waveguides by applying an electric field across the structure [11], but this requires additional manufacturing steps. These limitations do not exist in silicon nitride owing to its larger bandgap, providing a transparency window that extends to the ultraviolet [12]. In addition, the high index contrast to SiO_2 allows for high optical confinement with the option to tailor waveguide dispersion [13].

Indeed, wavelength conversion by FWM in Si_3N_4 waveguides has been presented previously. But in order to achieve high CE, a pulsed pump with high peak power has been used in straight waveguides [14]. Alternatively, cavity enhancement of a continuous-wave pump has been shown in resonating structures [15]. Comb generation by cascaded FWM has been demonstrated in [15–17]. These examples clearly indicate the potential of this material for nonlinear integrated optics. However, CW wavelength conversion in non-resonant silicon nitride waveguide structures has not been investigated thoroughly. In this Letter we present CW-pumped wavelength conversion using the waveguides previously developed in [18]. This work extends the research presented in [19] by providing additional measurements and a more detailed comparison with numerical simulations. These original waveguide designs featured low propagation loss [18] so that a large effective length L_{eff} of up to a few meters could be achieved in a compact platform. Larger interaction length results in an increased nonlinear phase shift and thus a higher FWM efficiency. We critically test the performance of these devices in a data conversion experiment that shows for the first time, to the best of our knowledge, CW-pumped wavelength conversion in a non-resonating Si_3N_4 waveguide.

The low propagation loss of this platform is achieved by using very thin waveguide dimensions. In this Letter we use a Si_3N_4 waveguide core cross section with a height of 100 nm and a width of 2.8 μm. The propagation loss is only 0.06 dB/cm. The waveguide cross section of the Si_3N_4 core and SiO_2 cladding is shown in Fig. 1(a). Waveguides with similar dimensions have been used previously for linear applications; design and fabrication were first presented in [18]. The weak field confinement

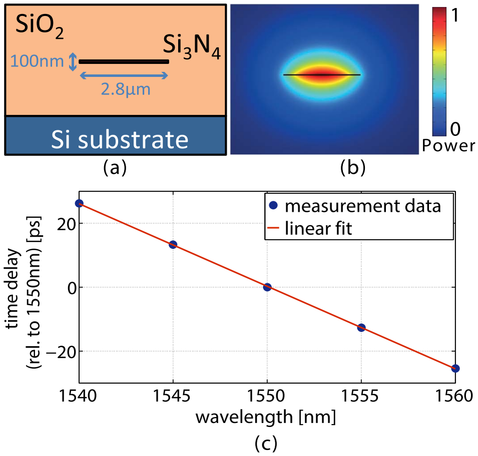

Fig. 1. (a) Schematic of waveguide cross section. (b) Simulation of power distribution of the fundamental TE-mode. (c) Measurement of time delay relative to 1550 nm versus wavelength.

in our design (only around 12% of the optical power is guided in the Si_3N_4 core) leads to low scattering interaction of the optical field with the thin waveguide sidewalls. The waveguide has single mode properties; simulations of the power distribution of the fundamental TE-mode are shown in Fig. 1(b). Since most of the power is in the cladding, we investigated the impact of having a change in its refractive index. A 5% variation of the cladding refractive index modifies the power confinement by less than 1.5%.

In the experiments, light is launched into the waveguide over tapered fibers with a coupling loss of 2.8 dB per facet. The propagation and coupling losses were evaluated with the cutback method. Waveguides of several meter lengths were coiled in spiral form with a minimum bending radius of 1 mm on a chip with a reduced footprint of 1.5 cm × 1.5 cm. As the waveguide has a polarization extinction ratio of more than 40 dB, we optimized the launched light for the lower-loss TE-polarization in all experiments. It is worth mentioning that even lower losses were achieved in the next generation of this platform, with thinner core thicknesses, with wafer bonding of high-quality thermal SiO_2, and at longer wavelengths, where the hydrogen bond absorption is lower [20], but the performance has not been tested for nonlinear optics.

The dispersion properties of this design were studied experimentally in a 6 m long waveguide by measuring the time delay versus wavelength using the time-of-flight technique. The results are presented in Fig. 1(c). From the measurement data we extracted a normal group velocity dispersion (GVD) of −0.4 ps/nm/m at 1550 nm and a dispersion slope of 1.4 ps/nm^2/m. The GVD is in fair agreement with the expected value of −0.56 ps/nm/m computed from mode solver simulations. We measured a nonlinear coefficient γ of 285 W/km for this low-loss Si_3N_4 waveguide in a dual pump experiment [21]. Compared to other techniques, the dual pump experiment amplifies the two pumps independently. Nonlinear effects occurring in the amplifiers become irrelevant. The results are in agreement with [10], where nonlinearities of different core thicknesses were investigated. To determine the optimal waveguide length for the following nonlinear experiments, we simulated the FWM-based idler generation by solving the nonlinear Schrödinger equation (NLSE) with the split-step Fourier method. As waveguide parameters for the simulations, we used the measured values of losses, dispersion, and nonlinear coefficient stated above. The simulated idler power as a function of waveguide length (Fig. 2) indicates that there is an optimum waveguide length of around 0.8 m. Above this length, a clear impact of the linear loss on the nonlinear FWM process is visible. For the theoretical model we used 33.3 dBm for the pump (1563 nm) and 18.9 dBm for the signal (1562 nm), which correspond to the power values used in the measurements. Next, we assessed the CE of the waveguides in an FWM experiment by launching a signal-pump pair into the waveguide in a degenerate pump configuration. A waveguide of 1 m length was used in this nonlinear measurement. To minimize the impact of dispersion, a detuning of 1 nm between the waves was chosen. Signal and pump were amplified independently and combined in a wavelength-division multiplexing coupler before launching into the waveguide. While keeping the signal at a constant 18.9 dBm, the pump power was varied. At the output of the chip, we analyzed the CE, optimistically defined as $P_{\mathrm{idler}}^{\mathrm{out}}/P_{\mathrm{signal}}^{\mathrm{out}}$, and the absolute idler power as a function of launched pump power. As expected, the maximum CE was −26.1 dB, corresponding to a launched pump power of 33.3 dBm as shown in Fig. 3(a). This results in a converted idler power of −19.6 dBm for the launched signal power of 18.9 dBm [Fig. 3(a)]. In the figure, measurement data are compared with the theoretical model, which shows a constant quadratic dependence on the pump power even up to 33.3 dBm. This indicates that the saturation effects owing to TPA or carrier effects are negligible. These CE results offer incomplete information about the absolute generated idler power. In spite of a relatively low CE, the advantage of our platform is that it can handle high CW power, thus allowing us to achieve high idler powers. The results presented here provide a 5.5 dB improvement with respect to the work in [19], where a 2 m long waveguide was used instead. This is in agreement with the simulations shown in Fig. 2.

An important aspect of any FWM-based wavelength converter is the impact of chromatic dispersion. We assess this by changing the wavelength spacing of the

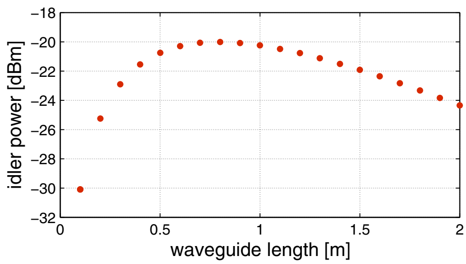

Fig. 2. Numerical simulation of maximum generated idler power versus length of waveguide.

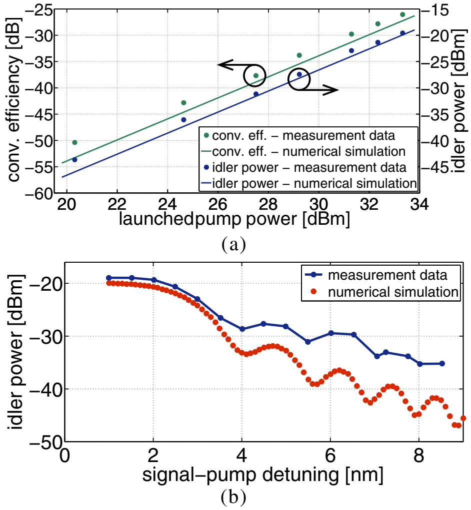

Fig. 3. (a) Measurement and numerical simulation of output conversion efficiency and idler power versus launched pump power in a 1 m long waveguide. (b) Measurement and numerical simulation of idler power versus wavelength separation of signal and pump.

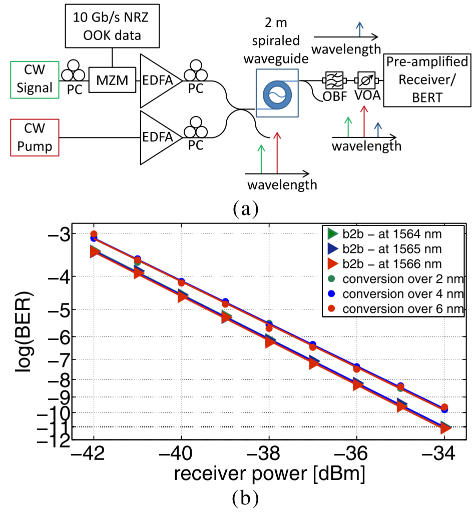

Fig. 4. (a) Schematic of experimental setup for BER measurements of data wavelength conversion (PC = polarization controller; MZM = Mach–Zehnder electro-optic modulator; EDFA = erbium-doped fiber amplifier; OBP = optical bandpass filter; VOA = variable optical attenuator; BERT = bit error rate tester). (b) BER curves for back-to-back (b2b) transmission and wavelength conversion over 2, 4, and 6 nm spacing.

signal-pump pair. Detuning signal and pump results in an additional phase mismatch that reduces the FWM CE. The launched power levels of signal and pump were kept constant at 18.9 and 33.3 dBm. The signal wavelength was decreased from 1562 nm while keeping the pump wavelength at 1563 nm. In Fig. 3(b) the results of the measured converted idler power versus signal-pump detuning are plotted. The 3 dB-bandwidth of the idler power is reached at a signal-pump spacing of 2.7 nm. We compared the measurements with the theoretical model of the system as shown in Fig. 3(b). Each point in the simulation curve is an independent solution of the NLSE for a different wavelength separation of signal and pump. The value of the GVD in the simulations is tuned to match the locations of the minimums in the measurement ripples.

Finally, to assess the performance of the waveguide in a more practical scenario, we carried out a wavelength data conversion experiment. The setup for this measurement is shown in Fig. 4(a). The signal wave is modulated with 10 Gb/s non-return-to-zero (NRZ) on-off keying (OOK) data, amplified, and then launched together with the amplified pump wave into a 2 m long waveguide. After the chip, the idler is filtered out from the spectrum with an optical bandpass filter (OBF) and launched into the receiver stage at different power levels, controlled with a variable optical attenuator (VOA). We use a pre-amplifier-based receiver stage in which the idler is optically amplified and filtered, and then amplified after the photo detector in the electrical domain. To evaluate the bit-error rate (BER) of the data conversion, we compared the data at the idler wavelength with the original generated bit sequence in front of the chip. Figure 4(b) shows the BER as a function of launched power into the pre-amplified receiver. Error-free (BER of 10^{-9}) data conversion is achieved at a receiver power of −34.6 dBm for up to 6 nm conversion width. A receiver penalty of 0.8 dB of converted data with respect to back-to-back (b2b) transmission can be seen. In comparison to data conversion in other platforms such as Si, where dispersion-engineered waveguides have been used [22], in our experiments the high normal dispersion significantly limits our conversion bandwidth. However, the waveguide dimensions in our design have not been optimized for high bandwidth wavelength conversion.

In summary, we have shown that the CMOS-compatible low-loss Si_3N_4 waveguide presented in [18], originally developed for linear optics applications, is also well suited for nonlinear optics applications (particularly FWM-based wavelength conversion). Although the nonlinear coefficient (285 W/km) is small compared to other integrated nonlinear platforms, we achieved an output CE of −26.1 dB and an absolute idler power of −19.6 dBm. Our experiments illustrate the relevance of having a long effective length and high power-handling capabilities. With these characteristics we present, for the first time, CW data conversion in a non-resonant Si_3N_4 waveguide.

This work is supported by the European Research Council under grant agreement ERC-2011-AdG-291618 PSOPA and the Wallenberg Foundation. Víctor Torres-Company gratefully acknowledges funding from the Swedish Research Council (VR).

References

1. H. Fukuda, K. Yamada, T. Shoji, M. Takahashi, T. Tsuchizawa, T. Watanabe, J. Takahashi, and S. Itabashi, Opt. Express **13**, 4629 (2005).

2. R. Salem, M. A. Foster, A. C. Turner, D. F. Geraghty, M. Lipson, and A. L. Gaeta, Nat. Photonics **2**, 35 (2007).
3. J. Leuthold, C. Koos, and W. Freude, Nat. Photonics **4**, 535 (2010).
4. Y. Shoji, T. Ogasawara, T. Kamei, Y. Sakakibara, S. Suda, K. Kintaka, H. Kawashima, M. Okano, T. Hasama, H. Ishikawa, and M. Mori, Opt. Express **18**, 5668 (2010).
5. D. J. Moss, R. Morandotti, A. L. Gaeta, and M. Lipson, Nat. Photonics **7**, 597 (2013).
6. D. Y. Oh, D. Sell, H. Lee, K. Y. Yang, S. A. Diddams, and K. J. Vahala, Opt. Lett. **39**, 1046 (2014).
7. B. Eggleton, B. Luther-Davies, and K. Richardson, Nat. Photonics **5**, 141 (2011).
8. P. Apiratikul, J. J. Wathen, G. A. Porkolab, B. Wang, L. He, T. E. Murphy, and C. J. K. Richardson, Opt. Express **22**, 26814 (2014).
9. C. Koos, P. Vorreau, T. Vallaitis, P. Dumon, W. Bogaerts, R. Baets, B. Esembeson, I. Biaggio, T. Michinobu, F. Diederich, W. Freude, and J. Leuthold, Nat. Photonics **3**, 216 (2009).
10. M. Tien, J. F. Bauters, M. J. R. Heck, D. J. Blumenthal, and J. E. Bowers, Opt. Express **18**, 23562 (2010).
11. A. Gajda, L. Zimmermann, M. Jazayerifar, G. Winzer, H. Tian, R. Elschner, T. Richter, C. Schubert, B. Tillack, and K. Petermann, Opt. Express **20**, 13100 (2012).
12. R. Soref, Nat. Photonics **4**, 495 (2010).
13. Y. Okawachi, K. Saha, J. S. Levy, Y. H. Wen, M. Lipson, and A. L. Gaeta, Opt. Lett. **36**, 3398 (2011).
14. J. S. Levy, A. Gondarenko, A. C. Turner-Foster, M. A. Foster, A. L. Gaeta, and M. Lipson, in *Proceedings of the Conference on Lasers and Electro-Optics/International Quantum Electronics Conference*, Baltimore, MD (Optical Society of America, 2009).
15. J. S. Levy, A. Gondarenko, M. A. Foster, A. C. Turner-Foster, A. L. Gaeta, and M. Lipson, Nat. Photonics **4**, 37 (2009).
16. F. Ferdous, H. Miao, D. E. Leaird, K. Srinivasan, J. Wang, L. Chen, L. T. Varghese, and A. M. Weiner, Nat. Photonics **5**, 770 (2011).
17. J. Pfeifle, V. Brasch, M. Lauermann, Y. Yu, D. Wegner, T. Herr, K. Hartinger, P. Schindler, J. Li, D. Hillerkuss, R. Schmogrow, C. Weimann, R. Holzwarth, W. Freude, J. Leuthold, T. J. Kippenberg, and C. Koos, Nat. Photonics **8**, 375 (2014).
18. J. F. Bauters, M. J. R. Heck, D. John, M. Tien, A. Leinse, R. Heideman, D. Blumenthal, and J. E. Bowers, in *Proceedings of European Conference on Optical Communication*, Turin, Italy (ECOC, 2010), paper We.8.E.6.
19. C. Krückel, V. Torres-Company, P. Andrekson, J. Bovington, J. Bauters, M. Heck, and J. Bowers, in *Proceedings of the Conference on Lasers and Electro-Optics*, San Jose, CA (Optical Society of America, 2014).
20. J. Bauters, M. J. R. Heck, D. D. John, J. S. Barton, C. M. Bruinink, A. Leinse, R. G. Heideman, D. J. Blumenthal, and J. E. Bowers, Opt. Express **19**, 24090 (2011).
21. A. Boskovic, S. V. Chernikov, J. R. Taylor, L. Gruner-Nielsen, and O. A. Levring, Opt. Lett. **21**, 1966 (1996).
22. N. Ophir, J. Chan, K. Padmaraju, A. Biberman, A. C. Foster, M. A. Foster, M. Lipson, A. L. Gaeta, and K. Bergman, IEEE Photon. Technol. Lett. **23**, 73 (2011).

Paper B

Linear and nonlinear characterization of low-stress high-confinement silicon-rich nitride waveguides

C. J. Krückel, A. Fülöp, T. Klintberg, J. Bengtsson, P. A. Andrekson and V. Torres-Company,

Optics Express, vol. 23, no. 20, pp. 25828-25837, 2015.

Linear and nonlinear characterization of low-stress high-confinement silicon-rich nitride waveguides

Clemens J. Krückel,[*] Attila Fülöp, Thomas Klintberg, Jörgen Bengtsson, Peter A. Andrekson, and Víctor Torres-Company

Photonics Laboratory, Department of Microtechnology and Nanoscience, Chalmers University of Technology, SE-412 96 Gothenburg, Sweden

[*]kruckel@chalmers.se

Abstract: In this paper we introduce a low-stress silicon enriched nitride platform that has potential for nonlinear and highly integrated optics. The manufacturing process of this platform is CMOS compatible and the increased silicon content allows tensile stress reduction and crack free layer growth of 700 nm. Additional benefits of the silicon enriched nitride is a measured nonlinear Kerr coefficient n_2 of $1.4 \cdot 10^{-18}$ m^2/W (5 times higher than stoichiometric silicon nitride) and a refractive index of 2.1 at 1550 nm that enables high optical field confinement allowing high intensity nonlinear optics and light guidance even with small bending radii. We analyze the waveguide loss ($\sim$1 dB/cm) in a spectrally resolved fashion and include scattering loss simulations based on waveguide surface roughness measurements. Detailed simulations show the possibility for fine dispersion and nonlinear engineering. In nonlinear experiments we present continuous-wave wavelength conversion and demonstrate that the material does not show nonlinear absorption effects. Finally, we demonstrate microfabrication of resonators with high Q-factors ($\sim 10^5$).

OCIS codes: (130.3120) Integrated optics devices; (130.7405) Wavelength conversion devices; (160.6000) Semiconductor materials; (190.4380) Nonlinear optics, four-wave mixing; (220.4241) Nanostructure fabrication; (230.5750) Resonators.

References and links

1. M. J. R. Heck, J. F. Bauters, M. L. Davenport, D. T. Spencer, and J. E. Bowers, “Ultra-low loss waveguide platform and its integration with silicon photonics,” Laser Photon. Rev. **8**(5), 667–686 (2014).
2. W. D. Sacher, Y. Huang, G. -Q. Lo, and J. K. S. Poon, “Multilayer silicon nitride-on-silicon integrated photonic platforms and devices,” J. Lightwave Technol. **33**(4), 901–910 (2015).
3. M. Piels, J. F. Bauters, M. L. Davenport, M. J. R. Heck, and J. E. Bowers, “Low-loss silicon nitride AWG demultiplexer heterogeneously integrated with hybrid III-V/Silicon photodetectors,” J. Lightwave Technol. **32**(4), 817–823 (2014).
4. R. Heiderman, M. Hoekman, and E. Schreuder, “TriPleX-based integrated optical ring resonators for lab-on-a-chip and environmental detection,” IEEE J. Sel. Top. Quantum Electron. **18**(5), 1583–1596 (2012).
5. M. Boerkamp, T. van Leest, J. Heldens, A. Leinse, M. Hoekman, R. Heiderman, and J. Caro, “On-chip optical trapping and Raman spectroscopy using a TripleX dual-waveguide trap,” Opt. Express **22**(25), 30528–30537 (2014).
6. J. F. Bauters, M. J. R. Heck, D. D. John, J. S. Barton, C. M. Bruinink, A. Leinse, R. G. Heiderman, D. J. Blumenthal, and J. E. Bowers, “Planar waveguides with less than 0.1 dB/m propagation loss fabricated with wafer bonding,” Opt. Express **19**(24), 24090–24101 (2011).

7. J. F. Bauters, J. R. Adleman, M. J. R. Heck, and J. E. Bowers, "Design and characterization of arrayed waveguide gratings using ultra-low loss Si_3N_4 waveguides," Appl. Phys. A **116**(2), 427–432 (2014).
8. D. T. Spencer, J. F. Bauters, M. J. R. Heck, and J. E. Bowers, "Integrated waveguide coupled Si_3N_4 resonators in the ultrahigh-Q regime," Optica **1**(3), 153–157 (2014).
9. M. Chavez-Boggio, D. Bodenmuller, T. Fremberg, R. Haynes, M. M. Roth, R. Eisermann, M. Lisker, L. Zimmermann, and M. Bohm, "Dispersion engineered silicon nitride waveguides by geometrical and refractive-index optimization," J. Opt. Soc. Am. B **31**(11), 2846–2857 (2014).
10. D. J. Moss, R. Morandotti, A. L. Gaeta, and M. Lipson, "New CMOS-compatible platforms based on silicon nitride and Hydex for nonlinear optics," Nature Photon. **7**(8), 597–607 (2013).
11. R. Halir, Y. Okawachi, J. S. Levy, M. A. Foster, M. Lipson, and A. L. Gaeta, "Ultrabroadband supercontinuum generation in a CMOS-compatible platform," Opt. Lett. **37**(10), 1685–1687 (2012).
12. J. S. Levy, A. Gondarenko, M. A. Foster, A. C. Turner-Foster, A. L. Gaeta, and M. Lipson, "CMOS-compatible multiple-wavelength oscillator for on-chip optical interconnects," Nature Photon. **4**(1), 37–40 (2010).
13. F. Ferdous, H. X. Miao, D. E. Leaird, K. Srinivasan, J. Wang, L. Chen, L. T. Varghese, and A. M. Weiner, "Spectral line-by-line pulse shaping of on-chip microresonator frequency combs," Nature Photon. **5**(12), 770–776 (2011).
14. T. Herr, K. Hartinger, J. Riemensberger, C. Y Wang, E. Gavartin, R. Holzwarth, M. L. Gorodetsky, and T. J. Kippenberg, "Universal formation dynamics and noise of Kerr-frequency combs in microresonators," Nature Photon. **6**(7), 480–487 (2012).
15. A. Gondarenko, J. S. Levy, and M. Lipson, "High confinement micron-scale silicon nitride high Q ring resonator," Opt. Express **17**(14), 11366–11370 (2009).
16. J. P. Epping, M. Hoekman, R. Mateman, A. Leinse, R. G. Heideman, A. van Rees, P. J. M. van der Slot, C. J. Lee, and K. -J. Boller, "High confinement, high yield Si_3N_4 waveguides for nonlinear optical applications," Opt. Express **23**(2), 642–648 (2015).
17. K. Luke, A. Dutt, C. B. Poitras, and M. Lipson, "Overcoming Si_3N_4 film stress limitations for high quality factor ring resonators," Opt. Express **21**(19), 22829–22833 (2013).
18. M. -C. Cheng, C. -P. Chang, W. -S. Huang, and R. -S. Huang, "Ultralow stress silicon rich nitride films for microstructure fabrication," Sens. Mater. **11**(6), 349–358 (1999).
19. T. Barwicz, M. A. Popovic, P. T. Rakich, M. R. Watts, H. A. Haus, E. P. Ippen, and H. I Smith, "Microring-resonator-based add-drop filters in SiN: fabrication and analysis," Opt. Express **12**(7), 1437–1442 (2004).
20. H. T. Philipp, K. N. Andersen, W. Svendsen, and H. Ou, "Amorphous silicon rich nitride optical waveguides for high density integrated optics," Electron. Lett. **40**(7), 419–421 (2004).
21. C. Krückel, A. Fülöp, P. Andrekson, and V. Torres-Company, "Continuous-wave nonlinear optics in low-stress silicon-rich nitride waveguides," in Proceedings of the Conferebce ib Optical Fiber Communications (2015), paper W1K.4.
22. K. Ikeda, R. E. Saperstein, N. Alic, and Y. Fainman, "Thermal and Kerr nonlinear properties of plasma-deposited silicon nitride/silicon dioxide waveguides," Opt. Express **16**(17), 12987–12994 (2008).
23. J. P. R. Lacey and F. P. Payne, "Radiation loss from planar waveguides with random wall imperfections," IEEE Proceedings J. **137**(4), 282–288 (1990).
24. M. Dinu, F. Quochi, and H. Garcia, "Third-order nonlinearities in silicon at telecom wavelengths," Appl. Phys. Lett. **82**(18), 2954–2956 (2003).
25. A. D. Bristow, N. Rotenberg, and H. M. van Driel, "Two-photon absorption and Kerr coefficients of silicon for 850-2200 nm," Appl. Phys. Lett. **90**(19), 191104-3 (2007).
26. G. E. Jellison, Jr. and F. A. Modine, "Parameterization of the optical functions of amorphous materials in the interband region," Appl. Phys. Lett. **69**(3), 371–373 (1996).
27. J. P. R. Lacey and F. P. Payne, "Optical Properties, Band Gap, and Surface Roughness of Si_3N_4," Phys. Stat. Solidi (A) **39**(2), 411–418 (1977).
28. V. P. Tzolov and M. Fontaine, "Nonlinear self-phase-modulation effects: a vectorial first-order perturbation approach," Opt. Lett. **20**(5), 456–458 (1995).
29. A. Boskovic, S. V. Chernikov, and J. R. Taylor, "Direct continuous-wave measurement of n_2 in various types of telecommunication fiber at 1.55 µm," Opt. Lett. **21**(24), 1966–1968 (1996).
30. M. -C. Tien, J. F. Bauters, M. J. R. Heck, D. J. Blumenthal, and J. E. Bowers, "Ultra-low loss Si_3N_4 waveguides with low nonlinearity and high power handling capability," Opt. Express **18**(23), 23562–23568 (2010).

1. Introduction

Silicon nitride (Si_xN_y) waveguides constitute a very attractive platform for integrated photonics applications. Similar to silicon-on-insulator (SOI) devices, their fabrication process is fully compatible with CMOS fabrication standards, and they render suitable for hybrid integration with other active components, such as modulators, amplifiers and detectors, both with silicon and III/V materials [1–3]. A key difference with respect to SOI is that the transparency window of Si_xN_y reaches into the visible and ultraviolet regions, which opens up new opportunities for integrated optics in life science applications [4, 5]. Ultra-low propagation losses of $\sim$0.1 dB/m in the optical telecommunication window have been reported for thin (40-50 nm), low confinement, Si_xN_y waveguides [6]. This has enabled the fabrication of high-performance passive devices, such as arrayed waveguide gratings [7] and ultra-high Q resonators [8] of relevance in fiber-optics applications.

Thicker waveguides provide higher optical confinement inside the waveguide core. High confinement allows for shorter curvature radii and, as a result, a higher density of photonic integration. In addition, the relatively high index contrast with respect to the silica cladding allows for engineering the dispersion of the waveguide (see e.g. [9]). This is crucial to achieve broadband phase matching in nonlinear optics applications [10]. Indeed, supercontinuum generation [9, 11], parametric frequency comb generation [12–14] and wavelength conversion [12] have been reported in thick Si_xN_y waveguides. In contrast to SOI waveguides, Si_xN_y shows no sign of two-photon absorption in the optical telecommunications band [10], which allows one to leverage the high-power erbium-doped fiber technology.

A challenge with Si_xN_y waveguides is that films thicker than $\sim$300 nm suffer large tensile stress and, in consequence, the waveguides tend to crack [15]. However, for a rectangular waveguide geometry, it is necessary to have very thick waveguides in order to get the zero dispersion wavelength in the telecommunications C-band [16]. Recent works address this manufacturability issue in different ways [16, 17]. In [17], mechanical trenches are inscribed in the oxide layer before the waveguide structures are fabricated. The trenches prevent further propagation of mechanical shock waves that initiate near the edge of the wafer. In this way, a crack-free region where devices can be safely fabricated, is cleared at the center of the wafer. With this method, stoichiometric Si_xN_y (i.e. Si_3N_4) waveguides as thick as 900 nm have been fabricated recently. Epping et al. [16] proposed an alternative method that consists of filling inscribed trenches in the oxide layer with silicon nitride. Hence the filled trench becomes the waveguide's core. Using Si_3N_4, they achieve propagation losses in the order of 0.4 dB/cm for waveguides of similar thickness.

An interesting feature of Si_xN_y films is that the relative content of Si and N can be precisely adjusted during the deposition process. A different composition in the film has a dramatic effect in the stress [18]. In particular, films with lower stress can be deposited by increasing slightly the content of silicon [19], resulting in crack-free, thick (>500 nm) waveguides as reported e.g. in [20]. In this work, we present a detailed analysis of the linear and nonlinear properties of our thick non-stoichiometric Si_xN_y waveguides [21]. Although the propagation losses ($\sim$1 dB/cm) are above the values reported by others [16, 17], the nonlinear Kerr coefficient is $\sim$5 times higher than stoichiometric Si_3N_4 waveguides [22], resulting in notable nonlinear effects even when operating with continuous-wave (CW) lasers. We provide an in-depth study of the dispersion and nonlinear characteristics and detail our fabrication process. We observe no sign of detrimental two-photon absorption effects in the telecommunications C-band. The high mode confinement allows for manufacturing high-quality factor resonators ($Q \sim 10^5$) with a free spectral range in the order of several nanometers, a record-high value for non-stoichiometric Si_xN_y waveguides. In essence, the presented structure combines in a single platform the beneficial features of stoichiometric silicon nitride (absence of two-photon absorption) with those of SOI waveguides (large nonlinear coefficient), making it very promising for integrated nonlinear optics applications.

The remaining of the work is structured as follows. In Section 2 we describe the fabrication process. Section 3 covers the loss characterization and the simulation results of group velocity dispersion, and the nonlinear coefficient are presented in section 4. In Section 5 nonlinear

#243801 Received 25 Jun 2015; revised 17 Sep 2015; accepted 17 Sep 2015; published 23 Sep 2015

experiments are presented, and in Section 6 we summarize the performance of our high-Q microresonators.

2. Fabrication

The manufacturing of the silicon-enriched nitride waveguides is compatible with the mature processing platform to fabricate complementary metal-oxide-semiconductor (CMOS) systems, which gives the option for mass production of integrated optics devices. A detailed schematic of the fabrication procedure of our Si_xN_y waveguides is presented in Fig. 1(a). To simplify matters, only the upper part of the wafer processing is shown so that the symmetric layer growth on the backside is not part of the schematic. Starting from a plain silicon wafer (P-doped/Boron, <100> orientation) in the first step, a 2 µm layer of buried-oxide is grown in a thermal wet oxidation process in H_2O environment. On top of the silicon dioxide film a layer of silicon-enriched nitride is deposited in a low-pressure chemical vapor deposition (LPCVD) process. By varying the gas composition of the film forming reactants NH_3 and SiH_2Cl_2 injected into the reaction chamber, the ratio of the silicon and nitrogen content in the Si_xN_y film can be adjusted. The recipe we used results in a ratio of around 65% silicon to 35% nitrogen that enables a tensile stress reduced growth of Si_xN_y films with a thickness of 700 nm. The film

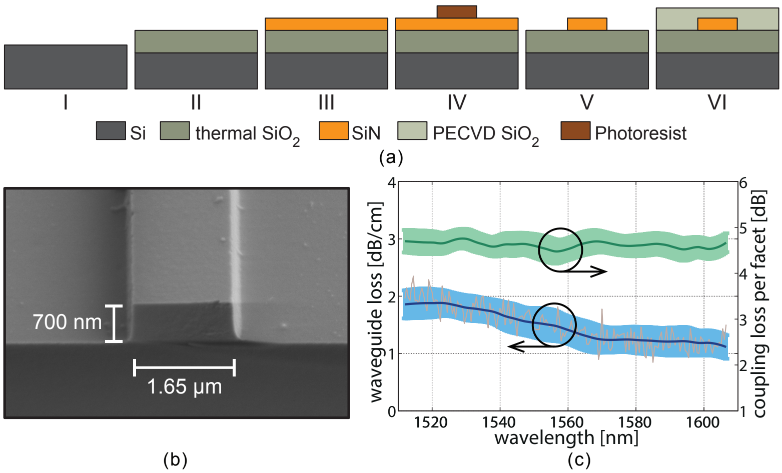

Fig. 1. (a) Schematic of fabrication process for silicon-enriched nitride waveguides. Only the processing of the top part of the wafer is presented. (I) Silicon wafer as initial condition. (II) Thermal wet oxidation of 2 µm SiO_2. (III) LPCVD deposition of 700 nm silicon-rich nitride in a gas mixture of NH_3 and SiH_2Cl_2. (IV) Patterning of the photoresist based etching mask by DUV lithography. (V) Dry etching of Si_xN_y in CHF_3 and O_2 and remaining etch mask removal. (VI) PECVD deposition of 2 µm SiO_2 in SiH_4 and N_2O. (b) SEM picture of patterned Si_xN_y strip after etching. Magnification of 70 000. (c) Experimental results of spectrally resolved waveguide loss and coupling loss in Si_xN_y waveguide (700 nm height, 1.65 µm width). The dark lines show the mean value, the bright shadowed areas the standard deviation and the brown curve shows the propagation loss for one sample waveguide, (see details in the text).

#243801 Received 25 Jun 2015; revised 17 Sep 2015; accepted 17 Sep 2015; published 23 Sep 2015

composition was measured with energy dispersive X-ray spectroscopy. In order to transfer the transverse waveguide pattern into the Si_xN_y layer we used a photoresist based soft mask during etching which is structured via deep-ultraviolet (DUV) contact lithography. This lithography technique readily enables to resolve feature sizes down to around 200 nm. The smoothness and durability of the etch mask is improved by a descum procedure and a heat treatment at 130 °C for 20 min. In a CHF_3 and O_2 based dry etching step, a Si_xN_y strip is etched with nearly smooth and vertical sidewalls as can be seen in the scanning electron microscope (SEM) picture in Fig. 1(b). The picture reveals that the 700 nm thick silicon-enriched nitride strip is crack free. With our DUV lithography and etching process a 400 nm gap between two waveguides can clearly be resolved as shown in Fig. 2(a). Finally, the 2 μm upper SiO_2 cladding of the waveguide is deposited in a plasma-enhanced vapor deposition (PECVD) step with SiH_4 and N_2O as the reactive gas mixture.

3. Loss characterization

To specify dominant loss contributions in our silicon-enriched nitride waveguides, we combined spectrally resolved transmission scans with the cut-back method. The transmission scans are measured by launching light from a tunable laser into the waveguide and sweeping the wavelength in synchronization with a photodetector to measure the system throughput for individual wavelengths. By calibrating the transmission scans, the fiber-to-fiber loss of the device under test were separated from additional setup loss. The wavelength scans with 189 data points were performed for three different waveguide lengths (1.98, 3.03, 5.01 cm). The transmission loss from three different lengths allows the fitting of a first-order polynomial, to extract propagation loss and coupling loss from the slope and offset of the polynomial. Performing an individual polynomial fit for each wavelength, results in a spectrally resolved characterization of the coupling and propagation loss. In Fig. 1(c) the waveguide propagation loss of one waveguide with 189 wavelength data points is shown. The noise of the curve, resulting from spurious reflection artifacts in the waveguide, was cleaned up using a moving

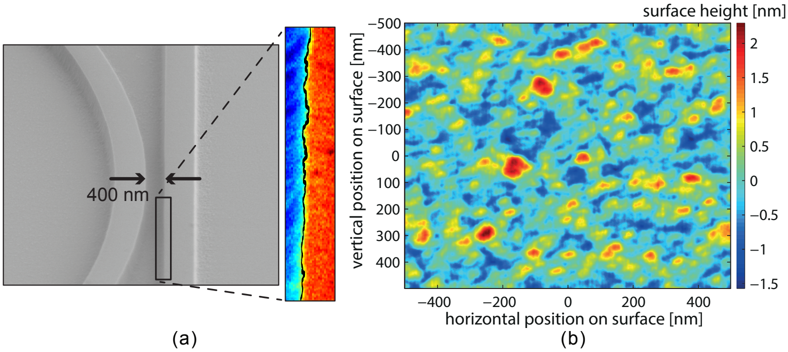

Fig. 2. (a) SEM picture of the coupling region between the bus waveguide and the microring resonator at a magnification of 25 000. The inset shows the indicated rectangular area for the analysis of sidewall roughness, with the SEM image intensity converted to color code. The black line going from top to bottom is the identified edge of the waveguide wall used to extract the roughness parameters. (b) Atomic force microscopy picture of the Si_xN_y surface.

#243801 Received 25 Jun 2015; revised 17 Sep 2015; accepted 17 Sep 2015; published 23 Sep 2015

average filter over 20% of the data points. In total, seven different waveguide systems at different locations in the same wafer were evaluated to calculate the mean value and standard deviation for the spectrally resolved propagation and coupling loss as presented in Fig. 1(c). It can be seen that the coupling loss is fairly constant over wavelength with a mean value of around 4.8 dB per facet owing to Fresnel reflections and modal field mismatch between the tapered fiber (spot size 2.5 μm) and the waveguide. The propagation loss decreases from around 1.8 dB/cm at 1510 nm down to 1.2 dB/cm above 1570 nm. This trend indicates dominant material loss over losses from scattering locations in the waveguide boundaries as the higher confinement at shorter wavelength increases the optical wave interaction with the material. The material losses in the C-band could be caused by higher-order vibrational modes of N-H bonds.

We support the claim of dominant material loss at lower wavelength by an estimation of the scattering losses which was done in two steps. First, the surface roughness of the waveguide sidewalls and the top surface was measured for the Si_xN_y waveguide strip after etching. The sidewall roughness was obtained from image processing the top-view SEM pictures of the straight waveguide; a result can be seen as the inset in Fig. 2(a) where the black meandering line indicates the detected position of the sidewall. For the top surface a two-dimensional surface profile was obtained with atomic force microscopy (AFM) and the results are presented in Fig. 2(b). From these measurements we calculated as indicators of the roughness feature size both the root mean square (rms) σ of the roughness height variations and the (auto-)correlation L_c of the fluctuations along the plane of surface. The extracted roughness parameters were (σ, L_c) = (5, 45) nm for the sidewall and (σ, L_c) = (0.5, 30) nm for the top surface. The bottom surface of the waveguide was not accessible for roughness measurements but it was assumed to have similar roughness parameters as for the top surface. In the second step the parameters were inserted into an expression for the scattering loss originally derived for slab waveguides [23]. It has, however, been widely used also for rectangular waveguides, with some reasonable though not entirely rigorous reinterpretation of the entities in the formula. Since our aim is to qualitatively compare the scattering losses to the total waveguide losses the precision in this approach should be more than sufficient. In addition to the surface roughness parameters, the scattering loss formula also contains some entities for the undisturbed waveguide - without surface roughness - which were obtained from numerical simulations as mentioned in the next section. The loss formula then yielded a total loss from the two sidewalls of $\sim$0.2 dB/cm and from the top and bottom interfaces of less than 0.01 dB/cm. The sidewall scattering loss is thus not insignificant but clearly smaller than the absorption loss, judging from the measurements of the total waveguide loss. The strong wavelength dependence of the total loss further underscores that absorption is the dominant loss mechanism, since the scattering loss is virtually independent of the wavelength; the simulations show that increasing the wavelength from 1500 to 1600 nm the sidewall scattering loss decreases by merely 0.01 dB/cm.

4. Simulation of group velocity dispersion and nonlinear coefficient

In order to receive realistic results from mode solver simulations the refractive indices of all three materials forming the waveguide were determined using spectroscopic ellipsometry over the wavelength range from 245 to 1690 nm. The measurements were taken from one point in the middle of the wafer. The measured refractive indices at 1550 nm for the thermally grown and PECVD deposited SiO_2 were around 1.44 and 1.46, and for the silicon-enriched nitride layer it was 2.1. Simulations were then carried out with a finite element method based solver (COMSOL). The high index contrast between core and cladding results in a power distribution mainly confined in the core as presented in Fig. 3(a), here presented for the fundamental

#243801 Received 25 Jun 2015; revised 17 Sep 2015; accepted 17 Sep 2015; published 23 Sep 2015

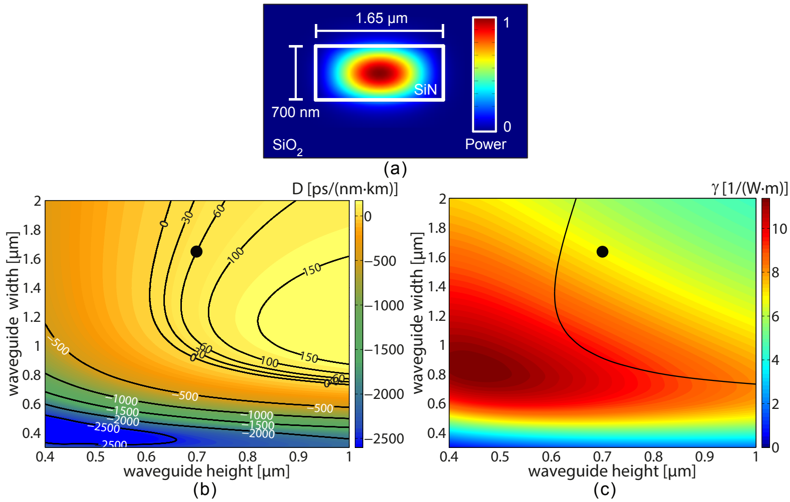

Fig. 3. (a) Simulation of power distribution of the fundamental TE-mode at 1550 nm wavelength. (b) Simulation of dispersion D as a function of waveguide height and waveguide width of the fundamental TE-mode at 1550 nm wavelength. The dot indicates the waveguide dimensions used in this publication. (c) Simulation of nonlinear parameter γ as a function of waveguide height and waveguide width of the fundamental TE-mode at 1550 nm wavelength. The dot indicates the waveguide dimensions used in this work and the black curve indicates the zero dispersion of the waveguide.

TE-mode at 1550 nm wavelength. The high confinement of this mode translates into a small effective area A_{eff} of around 0.9 µm^2 for a waveguide with dimensions of 700 nm in height and 1.65 µm in width. It is important to mention that for this cross-section dimension, both the fundamental and second order TE- and TM modes are guided for wavelengths above the L-band.
For efficient nonlinear processes over a wide spectrum a low and anomalous dispersion in the waveguide structure is essential. By tailoring the dimensions of the core medium, it is possible to change the waveguide dispersion in order to overcome the normal material dispersion to obtain the desired chromatic dispersion in the waveguide. For our material combination we studied the impact of the height and width of the waveguide on the dispersion D in detail. We varied the core dimensions with steps of 30 nm for the height and in steps of 90 nm for the width and interpolated the data to achieve fine resolved dispersion information for different waveguide cross sections as presented in Fig. 3(b) for the fundamental TE-mode at 1550 nm. The plot reveals that anomalous dispersion, $D > 0$, is achieved at waveguide dimensions thicker than 600 nm. With our stress reduced Si_xN_y, those thicknesses can be manufactured without film cracking, leading to high yield and reproducibility of the processed waveguides. The dimensions of the waveguides used in this work (1.65 µm width, 700 nm height) result in anomalous dispersion of around 60 ps/(nm·km) according to the simulations.
Nonlinear processes are enhanced with higher nonlinear parameter γ that is related to the nonlinear Kerr coefficient n_2, the wavelength λ of the optical field and the A_{eff} of the waveguide

#243801 Received 25 Jun 2015; revised 17 Sep 2015; accepted 17 Sep 2015; published 23 Sep 2015

Table 1. Comparison of nonlinear Kerr coefficient n_2 and optical band gap energy E_g for silicon, silicon-enriched nitride and stoichiometric silicon nitride.

		n_2 (at 1.5 μm) [m^2/W]	E_g [eV]
Si [24,25]	(100% Si)	$\sim 4 \cdot 10^{-18}$	1.12
Si_xN_y	(65% Si)	$1.4 \cdot 10^{-18}$	2.3
Si_3N_4 [22,27]	(43% Si)	$0.24 \cdot 10^{-18}$	~ 5

by

$$\gamma = \frac{2\pi n_2}{\lambda A_{\text{eff}}}. \tag{1}$$

Consequently, γ is enhanced by reducing the effective area and/or by increasing the nonlinear Kerr coefficient n_2 of the materials. We measured a nonlinear Kerr coefficient n_2 of $1.4 \cdot 10^{-18}$ m^2/W for the silicon-enriched nitride (see section 5). The comparison of our silicon-enriched nitride composition (65% Si, 35%N) to pure silicon (100% Si) and stoichiometric silicon nitride (43% Si, 57%N) shows that the value of our material falls in between the other two as shown in Table 1 [22, 24, 25]. This is expected taking into account that the increased content of silicon comes along with an increase in nonlinearities. But one should be aware of the drawback when increasing the silicon content in a Si_xN_y compound as the optical bandgap of the material is reduced. This increases the risk of two photon absorption (TPA) and the related carrier effects when working with high optical intensities.

The ellipsometry data of the Si_xN_y material absorption serves as the basis to fit a theoretical model based on the Tauc-Lorentz dispersion relationship as described in [26]. From the model a bandgap of 2.3 eV was inferred, which is between reported values for Si and Si_3N_4 presented in Table 1 [25, 27]. To bridge an optical bandgap energy of 2.3 eV with two photons of the same wavelength, each photon needs a wavelength of 1100 nm or shorter. This provides an indirect indication that in our material, TPA should be negligible in the C-band.

Utilizing the measured n_2 for Si_xN_y and the n_2 for silica available in the literature, the nonlinear parameter γ was simulated for different waveguide dimensions as presented in Fig. 3(c), which shows results for the fundamental TE-mode at 1550 nm. From the mode solver data the A_{eff} is calculated as in [28]. As can be seen in the plot, the maximum γ is achieved at waveguide dimensions of around 0.9 μm width and 450 nm height, where the optical field confinement leads to the smallest effective area. Comparing the simulations of the dispersion with the simulations of the nonlinear parameter indicates that there is a tradeoff between achieving anomalous dispersion and the highest nonlinearities. This tradeoff is highlighted by including the line of zero dispersion in the γ simulation graph in Fig. 3(c).

5. Nonlinear experiments

Next we show the potential of our platform in integrated optics by realizing a set of experiments with CW-pumped waveguides. The setup shown in Fig. 4(a) contains two tunable CW lasers where both waves are amplified independently and controlled in polarization. In this way we ensure that no nonlinear interaction occurs in the amplifiers but only in the integrated waveguide. The amplified spontaneous emission (ASE) of the signal after the amplifier is filtered out by an optical bandpass filter (OBF), whereas the ASE of the pump is removed in the 200 GHz bandwidth common port of the wavelength-division multiplexing (WDM) coupler. After combining signal and pump in the WDM coupler both waves are launched over a tapered fiber

#243801 Received 25 Jun 2015; revised 17 Sep 2015; accepted 17 Sep 2015; published 23 Sep 2015

into the microchip containing a straight waveguide of 0.94 cm length. The polarization of both waves is optimized for maximum throughput in the nonlinear experiments. After the chip the conversion efficiency (CE), defined as $P_{\text{idler}}^{\text{out}}/P_{\text{signal}}^{\text{out}}$, is analyzed with respect to signal and pump waves at the input. We experimentally demonstrate that the FWM conversion efficiency is directly proportional to the pump power, even at high power levels where the increased silicon content may raise the concern of TPA happening. In the experiments, signal and pump waves were placed with 1 nm wavelength separation (signal 1562 nm, pump 1563 nm) to minimize the impact of dispersion in the FWM process. The signal power was kept constant at 19 dBm as the pump power was increased. At the output the idler and signal power were tracked with an optical spectrum analyzer (OSA) and the conversion efficiency is displayed in Fig. 4(b). The agreement with the numerical simulation indicates that the nonlinear measurement results follow the theoretical dependence on the pump power. The deviation from a quadratic dependence is explained by the strong signal that saturates the FWM process slightly. The numerical simulations are realized by solving the nonlinear Schrödinger equation with the split-step Fourier method. Coupling loss variations are considered in the simulations.

The group velocity dispersion was studied in a second experiment. Here, the separation of signal and pump wavelength is changed by setting the pump to 1563 nm and detuning the signal away to shorter wavelengths. Both waves were launched into the waveguide at constant power levels (signal 19 dBm, pump 30 dBm). The change in CE over signal-pump detuning is plotted in Fig. 4(c). The graph indicates a 3 dB conversion bandwidth of around 8 nm. This corresponds to a dispersion value of ∼15 ps/(nm·km). The difference with respect to the simulation results [Fig. 3(b)] could be due to slight variations in the waveguide geometry that are within fabrication tolerance.

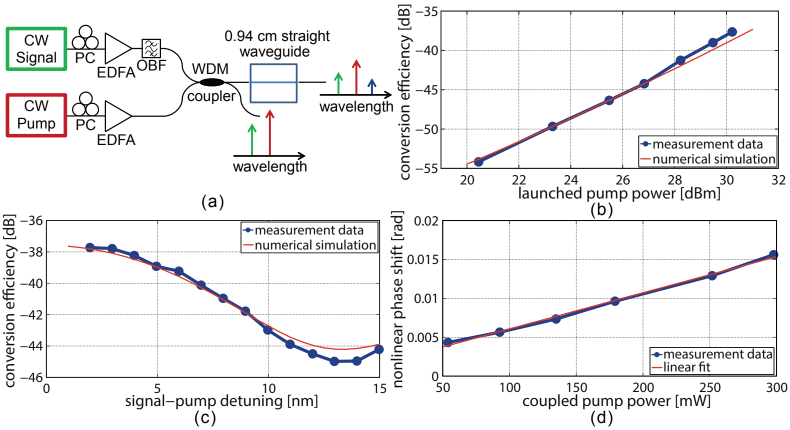

Fig. 4. (a) Schematic of experimental setup for four-wave mixing experiments. Continuous wave (CW) tunable laser. Polarization controller (PC). Erbium doped fiber amplifier (EDFA). Optical bandpass filter (OBF). Wavelength-division multiplexing (WDM) coupler. (b) Outcoupled conversion efficiency as a function of launched pump power into the waveguide. (c) Outcoupled conversion efficiency as a function of wavelength separation between signal and pump wave. (d) Nonlinear phase shift φ_{SPM} as a function of coupled pump power.

#243801 Received 25 Jun 2015; revised 17 Sep 2015; accepted 17 Sep 2015; published 23 Sep 2015

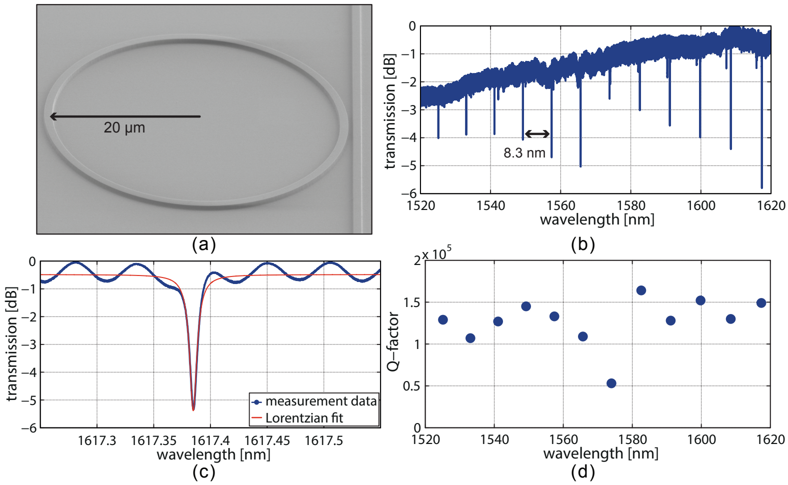

Fig. 5. (a) SEM picture of microring resonator with 20 µm bending radius at a magnification 7 000. (b) Wavelength dependent transmission spectrum of a 20 µm radius microring resonator system. (c) High-resolution scan of microring resonance at ~1617.4 nm. The quality factor is ~150 000. (d) Q-factor evaluation of resonances from 1520 to 1620 nm wavelengths.

Next, we provide a characterization of the nonlinear properties in a dual CW-pumped experiment with different launched power levels, as in [29, 30]. Two CW tunable lasers are co-polarized and amplified with high-power amplifiers. The generated idler power in the waveguide with a length of 0.94 cm depends on the amount of nonlinear phase shift φ_{SPM} according to:

$$\frac{I_0}{I_1} = \frac{J_0^2(\varphi_{SPM}/2) + J_1^2(\varphi_{SPM}/2)}{J_1^2(\varphi_{SPM}/2) + J_2^2(\varphi_{SPM}/2)}, \tag{2}$$

$$\varphi_{SPM} = \gamma L_{\text{eff}} P_{\text{in}}, \tag{3}$$

Here I_0 and I_1 are the intensities of the pump wave and the idler wave of first order. J_{i} corresponds to the i-th order Bessel function. The ratio of nonlinear phase shift φ_{SPM} versus coupled pump power into the waveguide is $4.64 \cdot 10^{-5}$ $(\text{mW})^{-1}$ as shown by the slope in Fig. 4(d). Following Eq. (3) and using a calculated effective length L_{eff} of 0.76 cm, a nonlinear coefficient γ of 6.1 $(\text{W}\cdot\text{m})^{-1}$ is evaluated. With an effective area A_{eff} of around 0.9 μm^2 the Kerr coefficient n_2 is thus $1.4 \cdot 10^{-18}$ m^2/W using Eq. (1).

6. Compact microstructures: ring resonator

The high index contrast between the SiO_2 cladding and the silicon-enriched nitride core facilitates the fabrication of ring resonator systems with small bending radii. We manufactured a ring resonator with 20 µm bending radius as shown in the SEM picture in Fig. 5(a) taken prior to the top cladding deposition. We characterized the ring by scanning a tunable laser across a broadband window (1520-1620 nm). Optimizing the polarization for maximum throughput leads to the transmission scan shown in Fig. 5(b). The measured free spectral range of the

#243801 Received 25 Jun 2015; revised 17 Sep 2015; accepted 17 Sep 2015; published 23 Sep 2015

resonances is 8.3 nm. A zoom-in on one of the resonances measured with 0.1 pm resolution is displayed in Fig. 5(c) indicating a quality factor of around 150 000 by fitting a Lorentzian curve and evaluating the full-width half maximum in linear scale. An evaluation of the quality factor for resonances in the wavelength regime between 1520 and 1620 nm is presented in Fig. 5(d) and shows Q-factors up to 165 000. These loaded quality factors are in agreement with the measured transmission loss in Fig. 1(c).

7. Conclusion

We have presented silicon enriched nitride waveguides with a composition of 65% silicon and 35% nitrogen and discussed the advantages of having enhanced silicon content in Si_xN_y with respect to Si_3N_4. The reduced tensile stress in the film allows thick film deposition and dispersion engineering towards anomalous dispersion, one important requirement for broadband wavelength conversion. Nonlinear characterization revealed a nonlinear Kerr coefficient n_2 of $1.4 \cdot 10^{-18}$ m^2/W and an optical bandgap of 2.3 eV that shows the potential for high power nonlinear optics as demonstrated experimentally. High confinement in the presented waveguides and propagation loss of $\sim$1 dB/cm enable high Q-factor ($\sim 1.5 \cdot 10^5$) ring resonators with small bending radii for high density of photonic integration. The waveguide loss has been evaluated to be dominated by material loss.

Acknowledgments

This work was supported by the European Research Council under grant agreement ERC-2011-AdG-291618 PSOPA, the Wallenberg Foundation and the Swedish Research Council (VR). The authors would like to thank Seyed Ehsan Hashemi for helping out with taking the AFM picture.